

Supplementary Information

Enhancing the kinetic and reversibility of copper batteries via anionic chemistry

Qianwei Zhou¹, Linyu Hu^{2*}, Huajun Zhang¹, Dongxu Hu¹, Guoqiang Liu³, Maowen Xu⁴, Hong Jin Fan⁵, Zhimeng Liu¹, Chunlong Dai^{3*}, and Xin He^{1*}

¹School of Chemical Engineering, Sichuan University, Chengdu 610207, China.

²College of Physics, Sichuan University, Chengdu 610065, China.

³College of Materials Science and Engineering, Sichuan University, Chengdu 610065, China.

⁴School of Materials and Energy, Southwest University, Chongqing 400715, China

⁵School of Physical and Mathematical Sciences, Nanyang Technological University, 637371, Singapore

E-mail: hulin13@sina.com; chunlongdai@scu.edu.cn; xinhe@scu.edu.cn

Section A. Materials

All reagents and solvents were of analytical grade and purchased from commercial suppliers including CuSO₄ (\geq 99%; Shanghai Titan Scientific Co., Ltd), Cu(ClO₄)₂·6H₂O (99.99%; Shanghai Titan Scientific Co., Ltd), CuBr₂ (99%; Shanghai Titan Scientific Co., Ltd), Cu(CH₃COO)₂ (98%; Shanghai Titan Scientific Co., Ltd), Cu(NO₃)₂·3H₂O (>99%; Shanghai Titan Scientific Co., Ltd), CuCl₂ (98%; Shanghai Titan Scientific Co., Ltd), Mn(ClO₄)₂·6H₂O (>98%; Shanghai Titan Scientific Co., Ltd), acrylamide (AR; Chengdu Kelong Chemical Reagent Co. Ltd), ammonium persulfate (98%; Adamas-beta), N,N'-Methylenebisacrylamide (99%; Adamas-beta), N,N,N',N'-tetramethylethylenediamine (99%; Adamas-beta), graphite paper (Changsha Spring Co., Ltd), and used without further purification. The Cu foil (50 μ m; Hefei Wenghe Metal Materials Co., Ltd.) and Ti foil (20 μ m; Hefei Wenghe Metal Materials Co., Ltd.) were cleaned with ethanol and dried before use.

Section B. Experimental section

Preparation of electrolytes. 0.5 m Cu(ClO₄)₂ electrolyte was prepared by dissolving 0.5 mmol Cu(ClO₄)₂·6H₂O in 1 g deionized water (denoted as: 0.5 m Cu(ClO₄)₂). Other electrolytes with different anions were prepared similarly except for using CuSO₄, CuBr₂, Cu(CH₃COO)₂, Cu(NO₃)₂·3H₂O, and CuCl₂ as copper salts. Different concentrations of Cu(ClO₄)₂ electrolytes were prepared by dissolving varying amounts of Cu(ClO₄)₂·6H₂O in deionized water with concentrations of 1 m, 2 m, 3 m, 4 m, and 5 m, respectively.

Preparation of hydrogel electrolytes. First, 6 g of acrylamide was dissolved in 20 mL of deionized water while stirring to create a uniform solution. Following this, ammonium persulfate (20 mg), N,N'-Methylenebisacrylamide (3 mg), and N,N,N',N'-tetramethylethylenediamine (15 μ L) were added into the initiate polymerization under continuous stirring. Then, the mixed solution was quickly transferred into a PTFE mold, after sealing and reacting at 50 °C for 12 hours to obtain polyacrylamide (PAM) hydrogel. The PAM hydrogel underwent drying at 80 °C for an additional 12 hours to obtain dry PAM gel. Finally, the dry PAM gel was soaked in 3 m Cu(ClO₄)₂ + 1 m Mn(ClO₄)₂ electrolyte for 3 days to obtain the hydrogel electrolyte.

Preparation of planar interdigitated Cu-MnO₂ micro-batteries. Graphite paper (negative current collector) and Cu foil (positive current collector) were adhered to polyimide tape.

Following this, interdigitated microelectrodes were created using the laser engraving method. Each microelectrode has a width of approximately 500 μm , a length of 0.3 cm, and a spacing of 300 μm between adjacent fingers. Eventually, 2 mm thick hydrogel electrolyte was coated onto the microelectrode to acquire the planar interdigitated Cu-MnO₂ micro-batteries.

Section C. Methods

Material characterizations. X-ray diffraction (XRD) measurements were performed on a Haoyuan DX-2800 High-Resolution Diffractometer with Cu Ka radiation ($\lambda = 1.54051 \text{ \AA}$) in the range of 20°~80°. The morphologies of the Cu electrode and MnO₂ electrode were characterized by scanning electron microscopy (SEM, JSM 7610F, JEOL Ltd., Japan) operated at 15 kV. Raman spectroscopy for electrolytes was conducted on a Horiba LabRAM HR Evolution microscope with a 532 nm laser. In situ optical microscopy was conducted on an Olympus BX43 microscope. Fourier transform infrared spectroscopy (FTIR) analysis was performed using a Nicolet iS50 FTIR spectrometer in the wavenumber range from 4000 to 400 cm^{-1} at a resolution setting of 4 cm^{-1} . The pH values of different salt solutions were measured with a precision pH meter (PHS-3C) at room temperature.

Electrochemical measurements. Electrochemical tests of Cu||Cu and Cu||Ti cells were assembled in 2032-type coin cells. Cu and Ti foil, each with a diameter of 12 mm, were employed as the electrodes, and a glass fiber separator (GE-Whatman) was used. The cells were assembled in an open environment with 120 μL electrolyte. The galvanostatic charge/discharge (GCD) curves, rate capability and cycling performance were recorded on a Neware battery charge/discharge system (Neware, Shenzhen, China). Cyclic voltammetry (CV), Linear sweep voltammetry (LSV), chronoamperometry (CA) and electrochemical impedance spectroscopy (EIS) were conducted on the Metrohm VIONIC electrochemical workstation. CV curves of Cu||Ti cells were measured within the voltage window from -0.3 to 0.5 V. EIS spectra were conducted in the temperature range of 30 °C to 50 °C and the frequency range of 0.01 Hz to 100 Hz. LSV tests were performed in a two-electrode configuration, in which stainless steel foil as working electrode, Cu foil as the reference and counter electrode, and scan rate is 1.0 mV s^{-1} . The corrosion potential and current density were calculated using a linear fit of Tafel plots in Cu||Cu cells at 2.0 mV s^{-1} . The long-term low-temperature performance was tested in a bench-top type temperature chamber JL-E702-100B70. The ionic conductivity (σ) of

electrolytes at different temperatures was calculated by the Eq. 1: s

$$\sigma = \frac{d}{R \times S}$$

where d, R, and S are the thickness, the resistance, and the contact area with the electrode, respectively.

The activation energy (Ea) of the electrolytes was estimated by the fitting of Arrhenius equation (Eq. 2 and Eq. 3):

$$\sigma(T) = Ae^{-\frac{E_a}{RT}}$$

$$\ln \sigma(T) = \ln A - \frac{E_a}{RT}$$

where T is the temperature, R is the Boltzmann constant, and A is a constant.

The transference number of Cu²⁺ ($t_{Cu^{2+}}$) was determined by the following equation:

$$t_{Cu^{2+}} = \frac{I_s(\Delta V - I_0 R_0)}{I_0(\Delta V - I_s R_s)}$$

where ΔV is the applied voltage (25 mV), I_0 and R_0 are the initial current and resistance, respectively; I_s and R_s are the steady-state current and resistance, respectively.

Section D. Computational Methods.

Molecular dynamics (MD) simulations for the electrolyte structures were performed using the Force module with COMPASS III force field^{1,2} in Materials Studio (MS) 2020. The numbers of water molecules and ions are provided in Table S4. Geometry optimization was first conducted to relax the initial system with ultrafine quality settings (energy convergence tolerance: 2.0×10^{-5} kcal mol⁻¹, force tolerance: 1×10^{-3} kcal mol⁻¹ Å⁻¹). After energy minimization, NPT runs were performed at 300 K for 5 ns to ensure the system equilibrium. Then, another 5 ns simulation under the NVT ensemble was carried out for analysis. The diffusion coefficients of Cu²⁺ can be estimated from the slope of the mean square displacement (MSD) curves by the Einstein relationship³ and analyzed through the last 2.5 ns simulation.

Gaussian 16W software⁴ was used to perform the binding energy calculations within the density functional theory (DFT) framework. All molecular structures were computed using the B3LYP (Becke, three-parameter, Lee–Yang–Parr) hybrid functional.⁵ The effective core pseudopotentials were used to treat the core electrons. For the high-level B3LYP computations, two basis sets were employed: the LANL2DZ^{6,7} basis set was used for the Cu atom, while the

6-311++G(d,p)⁸ basis set was applied to O, H, S, N, Cl, Br, and C atoms.

Section E. Supplementary Figures

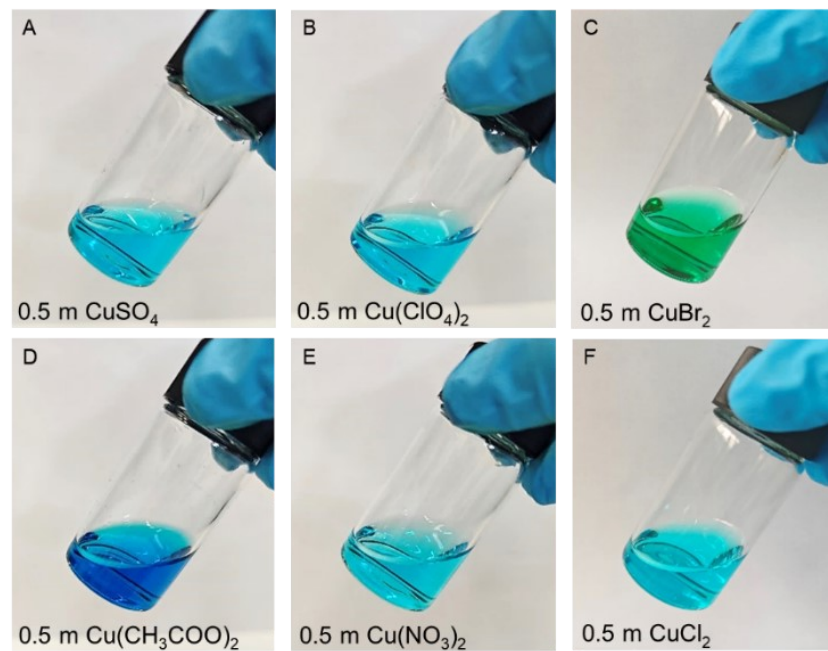


Fig. S1 Photographs of the prepared various aqueous copper ion electrolytes.

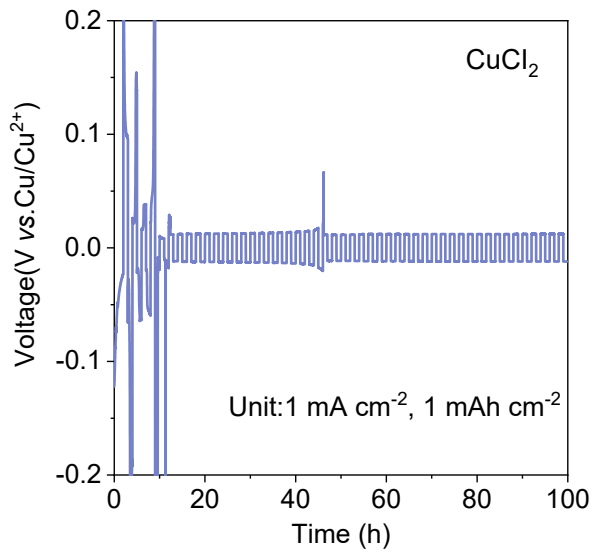


Fig. S2 Voltage profiles of symmetric cells in 0.5 m CuCl_2 electrolytes at 1 mA cm^{-2} with 1 mAh cm^{-2} .

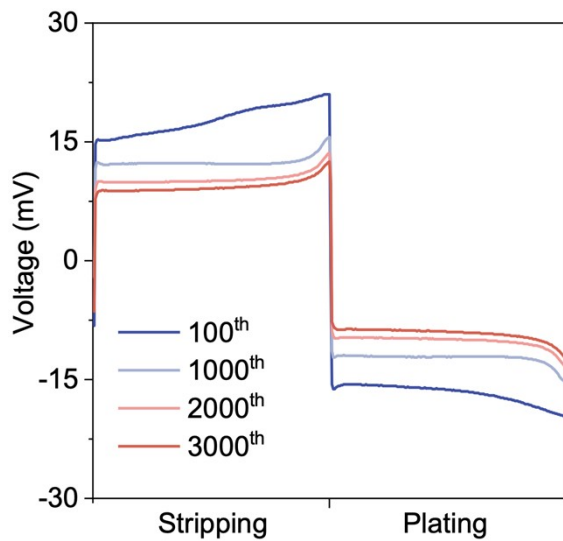


Fig. S3 Partially enlarged voltage profiles obtained in $\text{Cu}(\text{ClO}_4)_2$ electrolyte at various cycles in $\text{Cu}||\text{Cu}$ cells.

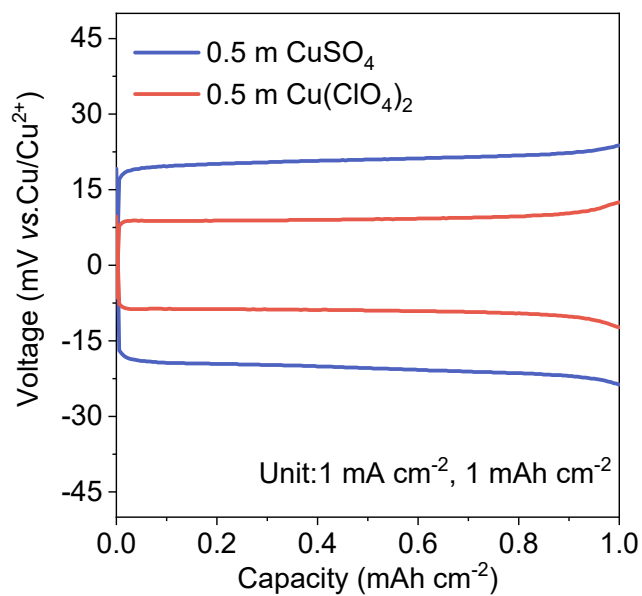


Fig. S4 Voltage profiles of Cu plating/stripping at 1 mA cm^{-2} with a capacity of 1 mA h cm^{-2} .

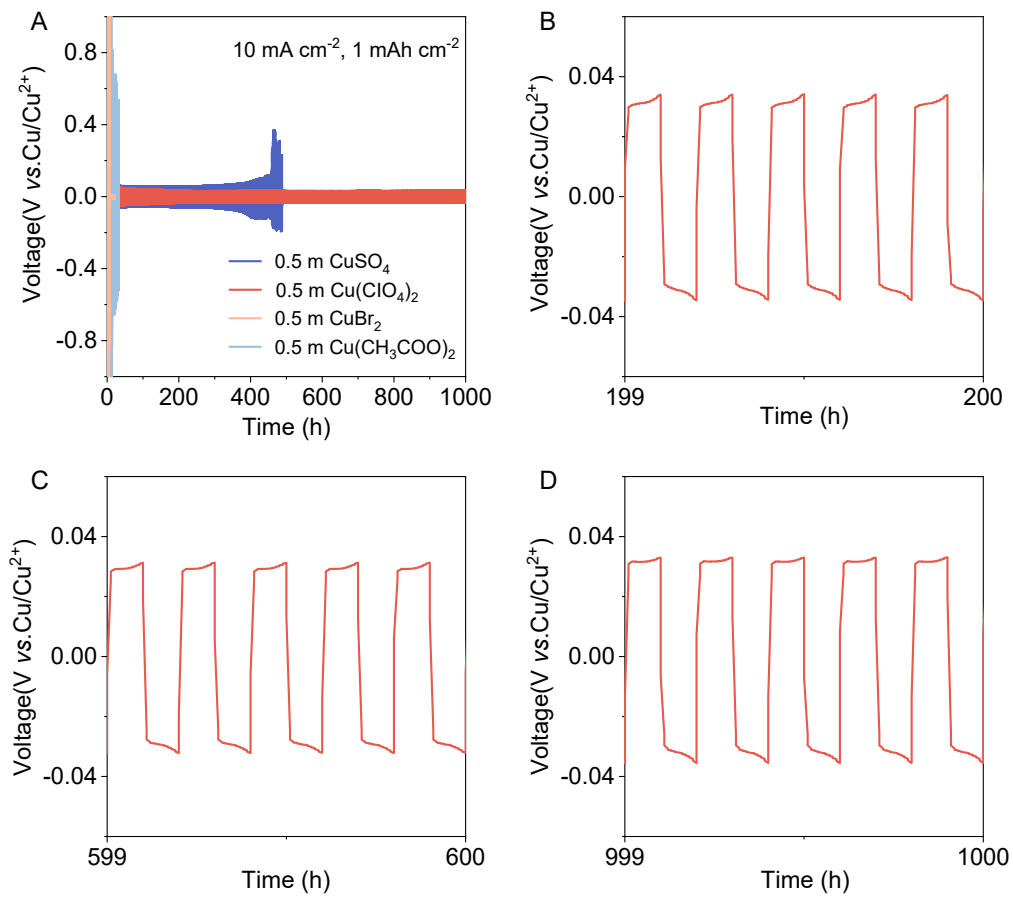


Fig. S5 (A) Voltage profiles of symmetric Cu||Cu cells with different electrolytes at 10 mA cm⁻². (B-D) Enlarged voltage profiles of Cu||Cu cell with 0.5 m Cu(ClO₄)₂ electrolyte at different cycling stages.

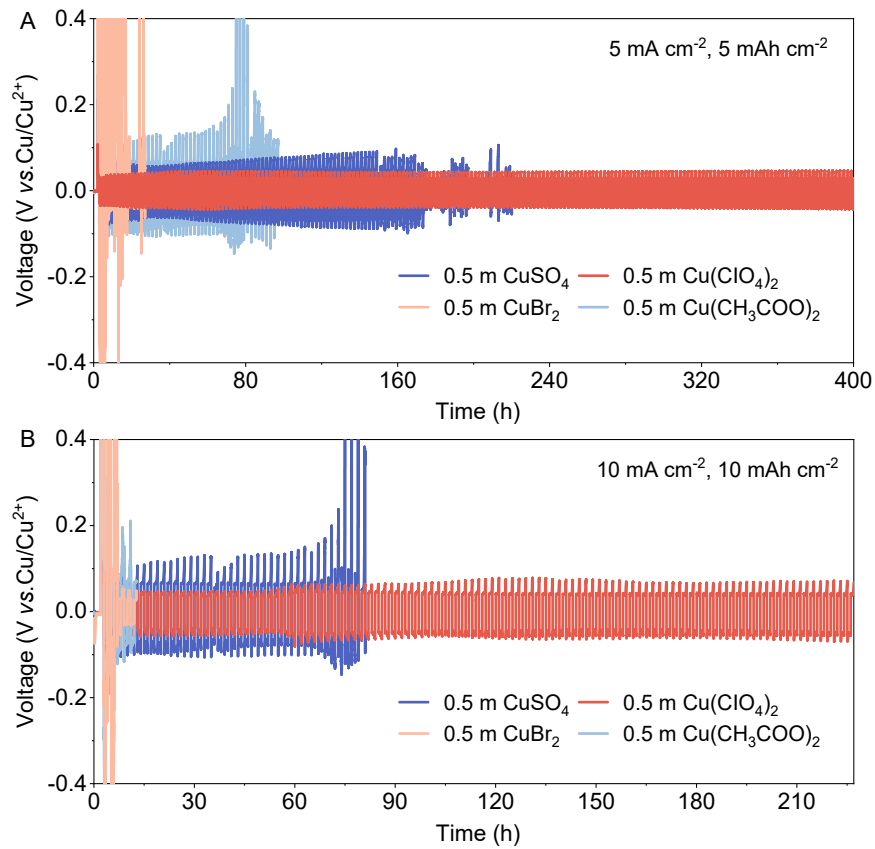


Fig. S6 Long-term cycling stability of Cu||Cu symmetric cells at (A) 5 mA cm⁻² with a capacity of 5 mA h cm⁻² and (B) 10 mA cm⁻² with a capacity of 10 mA h cm⁻².

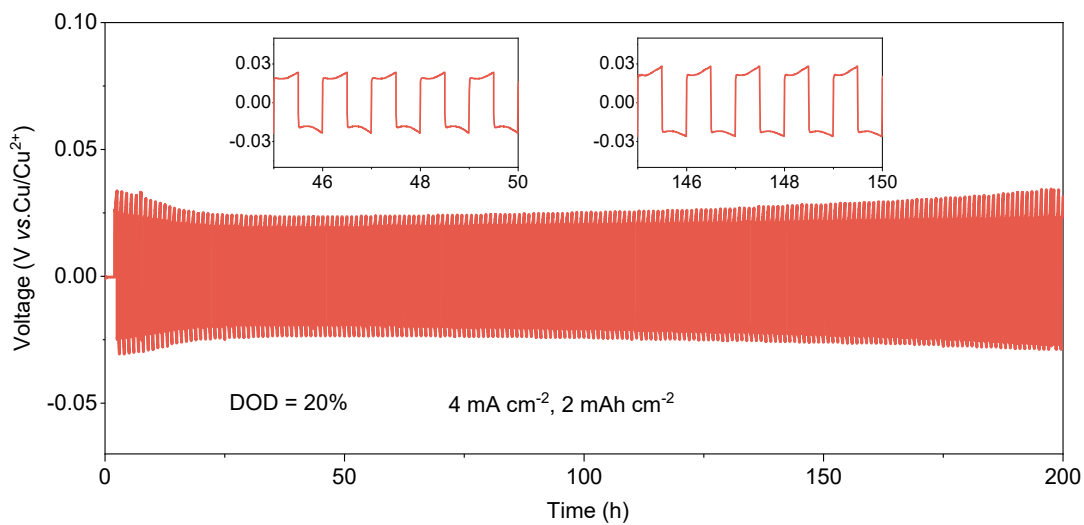


Fig. S7 Cycling performance of symmetric cells with $\text{Cu}(\text{ClO}_4)_2$ electrolyte at DOD of 20%.

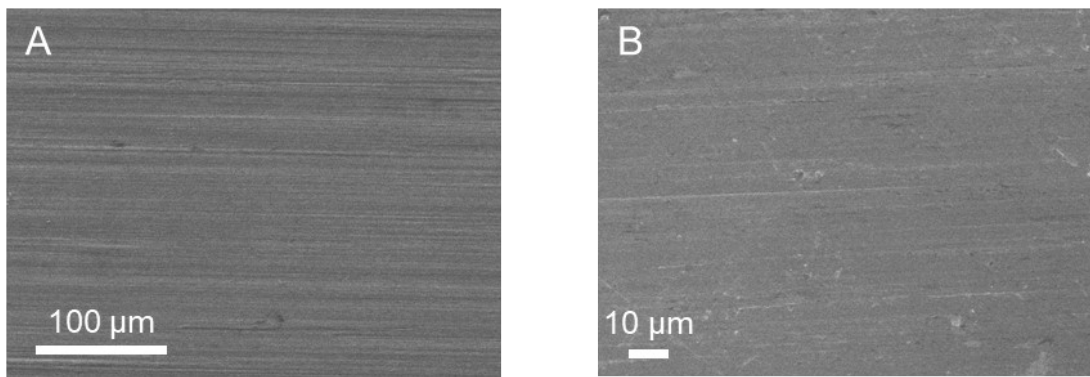


Fig. S8 SEM images of the Cu foil.

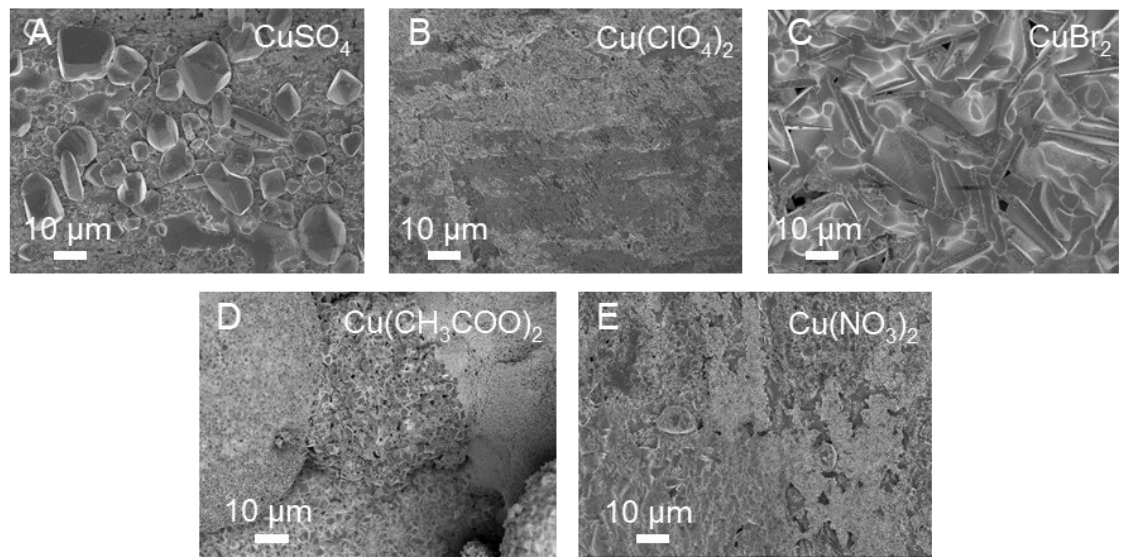


Fig. S9 SEM images of cycled Cu electrodes in different electrolytes.

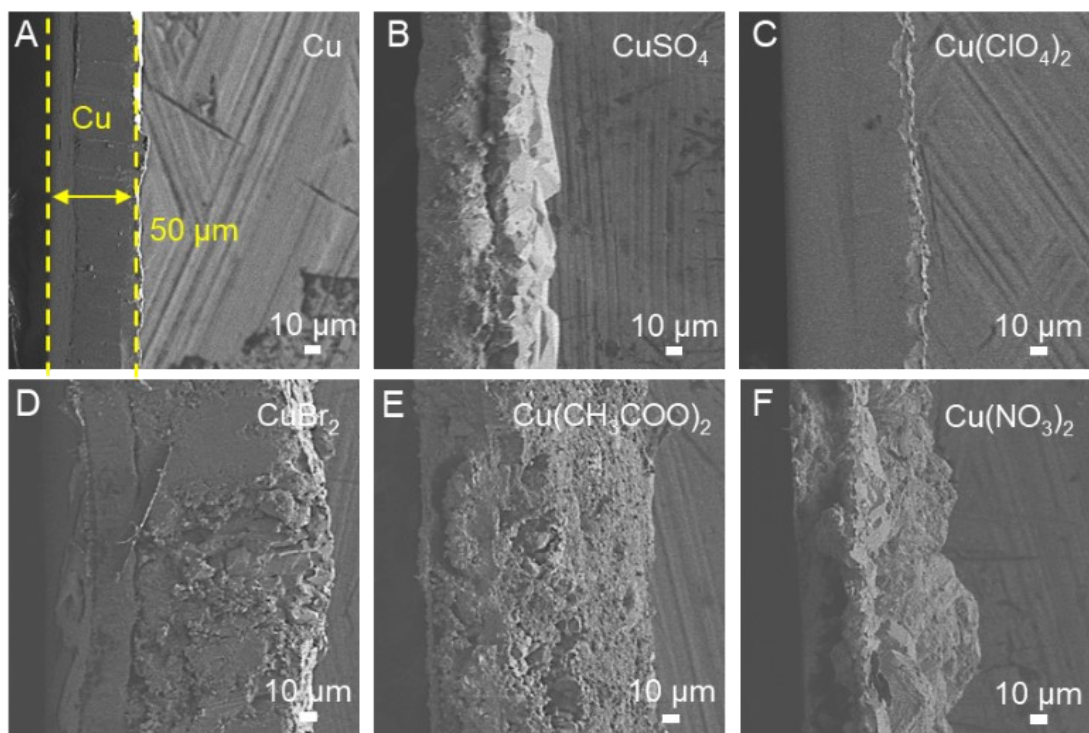


Fig. S10 Cross-sectional SEM images of (A) pristine Cu and (B-F) Cu electrodes cycled in various electrolyte after 100 cycles.

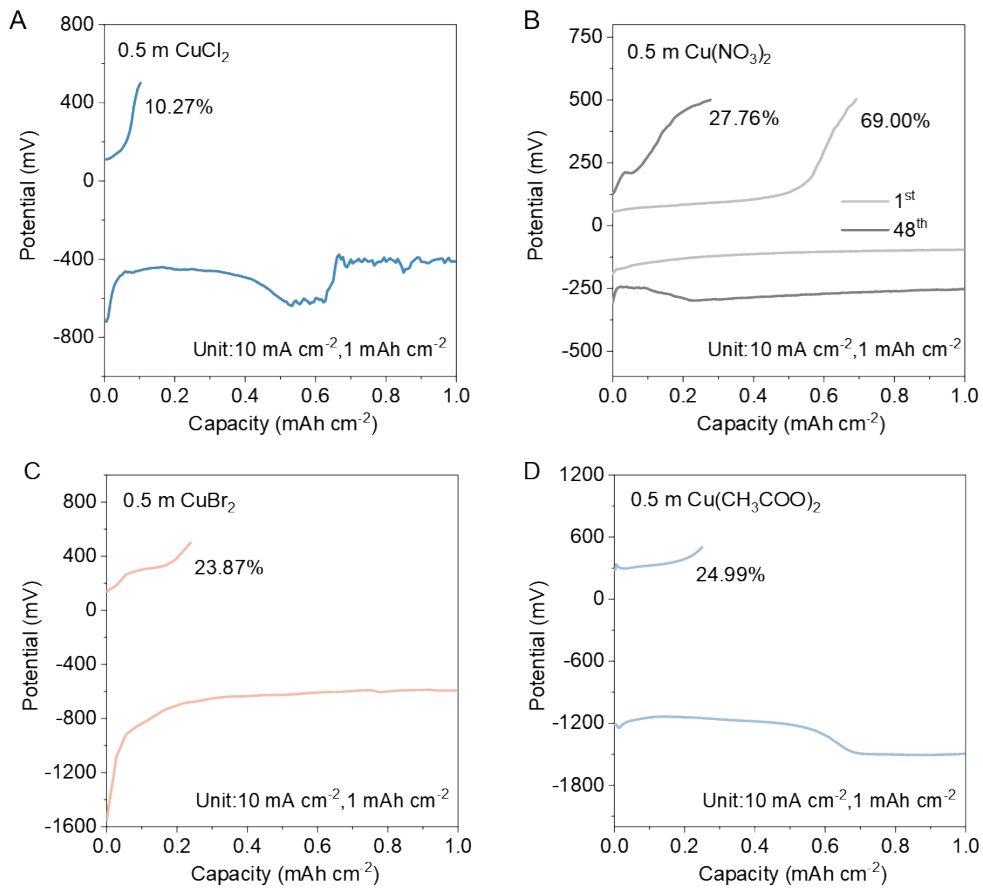


Fig. S11 Initial voltage profiles of $\text{Cu}||\text{Ti}$ cells at 10 mA cm^{-2} in (A) 0.5 m CuCl_2 , (B) $0.5 \text{ m Cu}(\text{NO}_3)_2$, (C) 0.5 m CuBr_2 , and (D) $0.5 \text{ m Cu}(\text{CH}_3\text{COO})_2$ electrolytes.

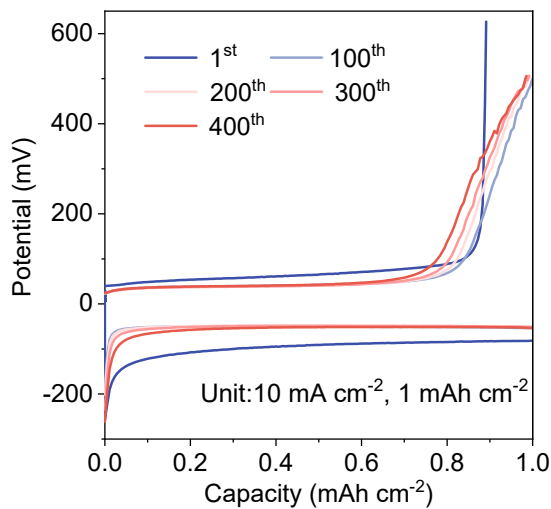


Fig. S12 Voltage profiles of different cycles in $\text{Cu}(\text{ClO}_4)_2$ electrolyte.

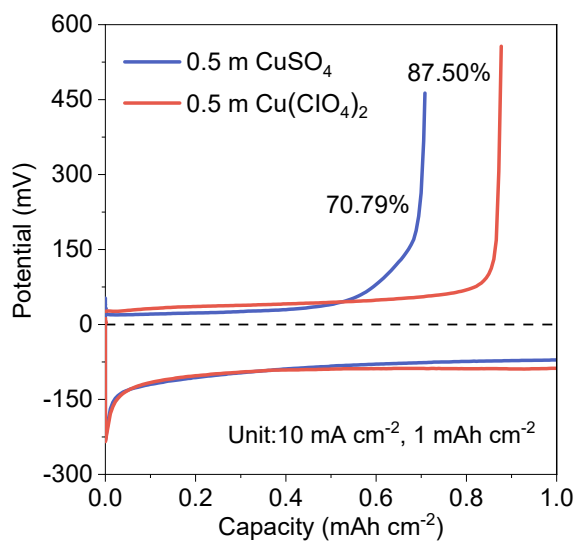


Fig. S13 Initial voltage profiles and CEs in 0.5 m CuSO_4 and $0.5 \text{ m Cu}(\text{ClO}_4)_2$ electrolytes at 10 mA cm^{-2} .

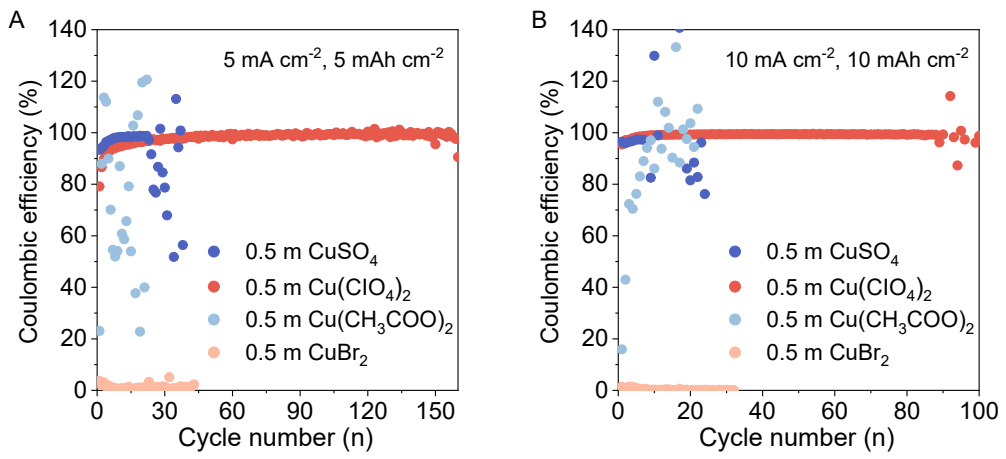


Fig. S14 Long-term cycling stability of Cu||Ti asymmetric cells with various electrolytes at (A) 5 mA cm^{-2} with a capacity of 5 mA h cm^{-2} and (B) 10 mA cm^{-2} with a capacity of 10 mA h cm^{-2} .

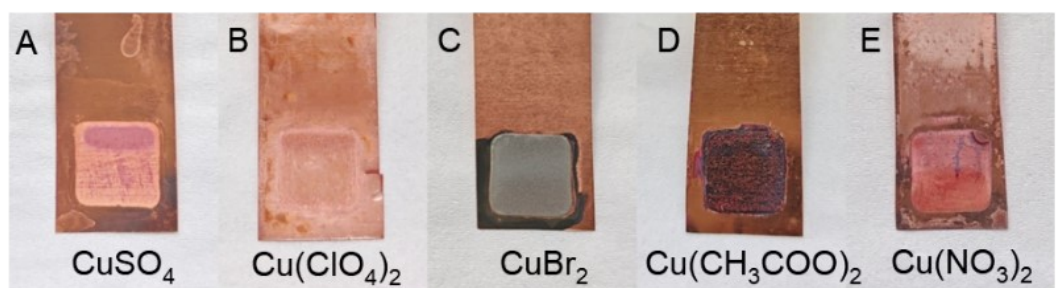


Fig. S15 Optical images of Cu electrodes cycled in various electrolytes.

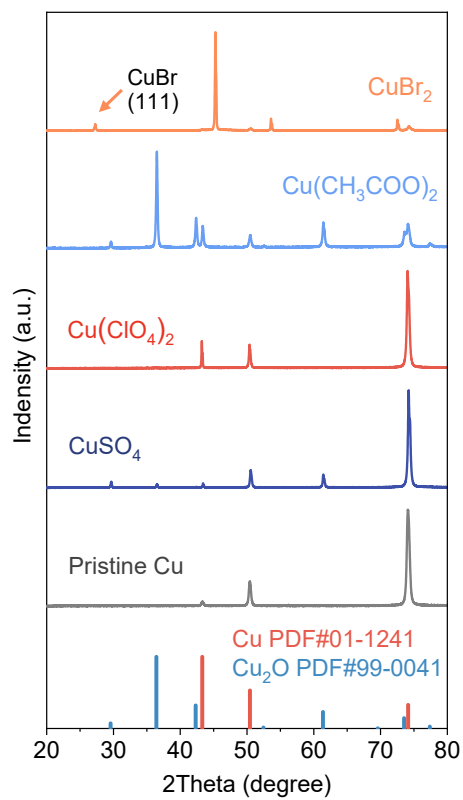


Fig. S16 XRD pattern of Cu electrode after 50 cycles in different electrolytes.



Fig. S17 Optical images of Cu foils immersed in different electrolytes for 5 days.

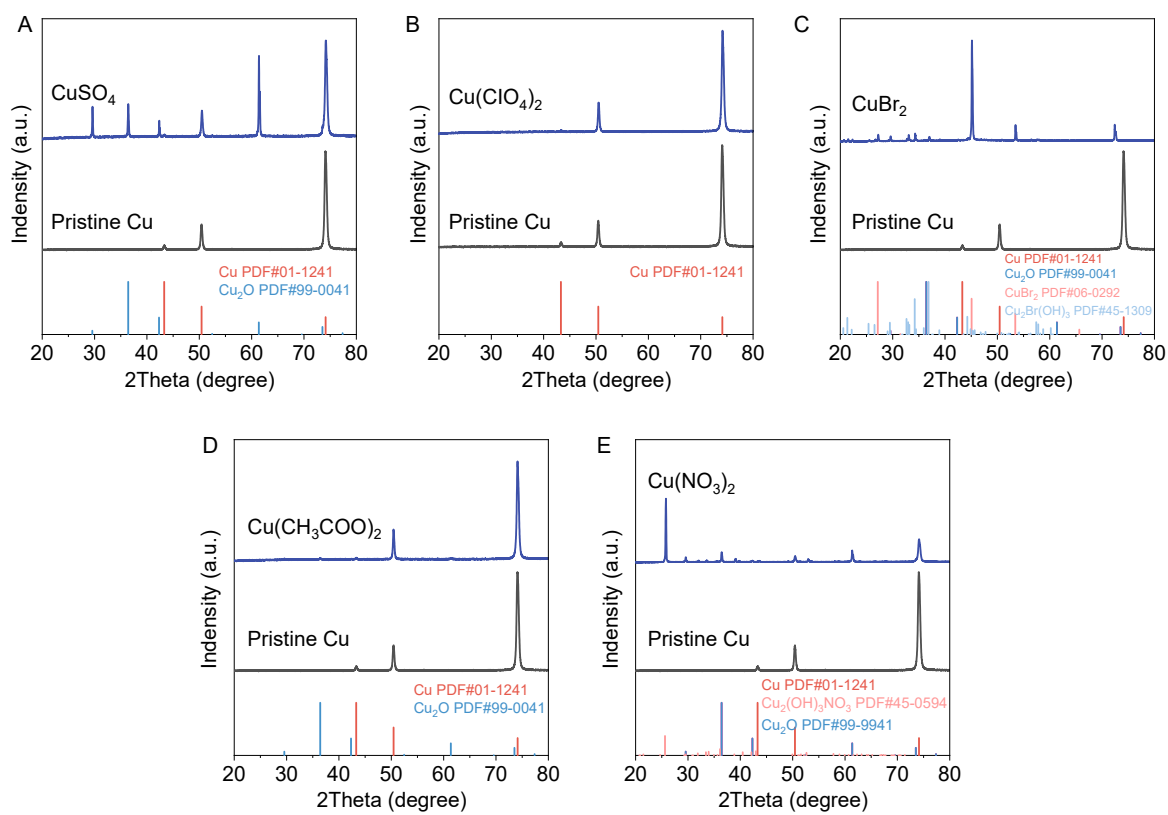


Fig. S18 XRD patterns of Cu foils immersed in different electrolytes for 5 days.

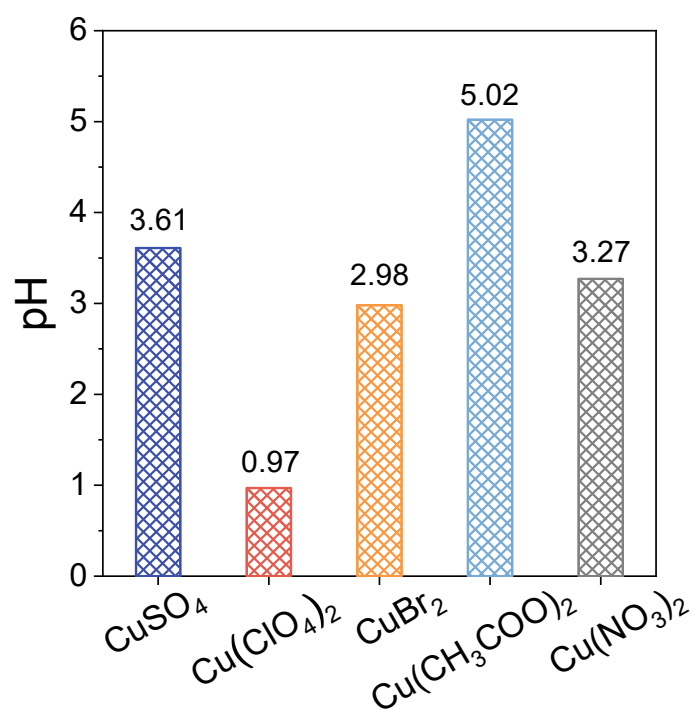


Fig. S19 pH value of five electrolytes at a concentration of 0.5 m.

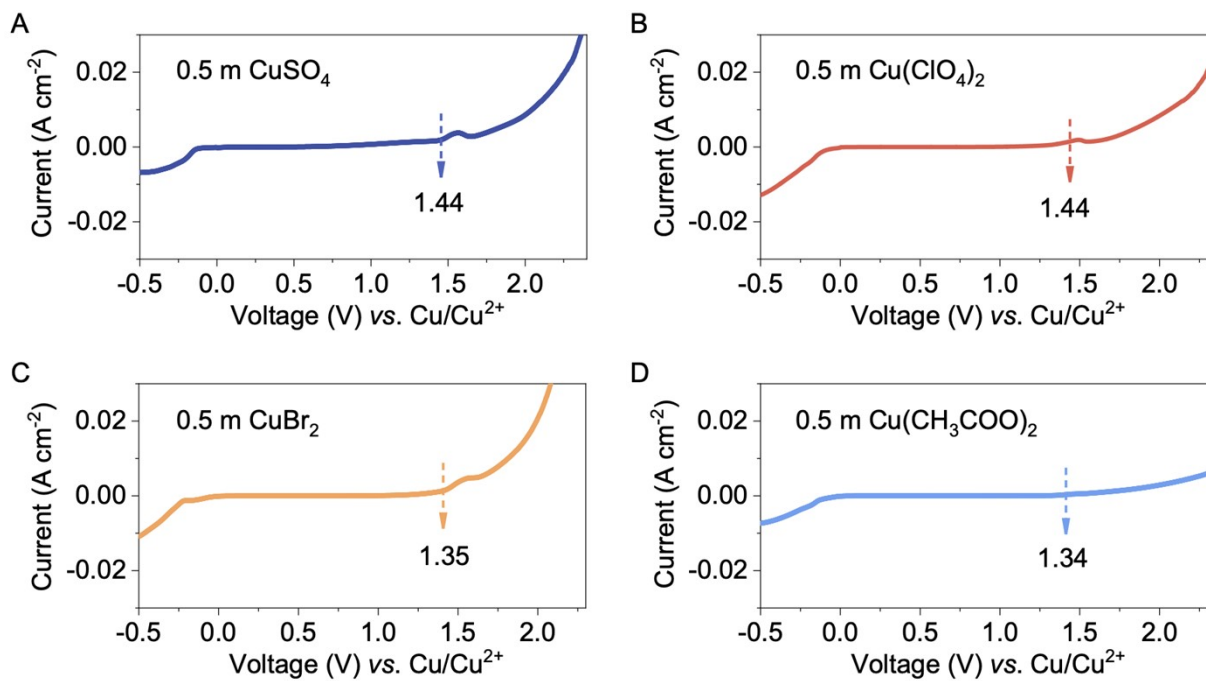


Fig. S20 LSV curves for electrochemical window of different electrolytes at a scan rate of 1 mV s^{-1} .

The decrease in current near 0 V (vs. $\text{Cu}^{2+}/\text{Cu}^0$) is attributed to the reduction of Cu^{2+} ions to Cu.

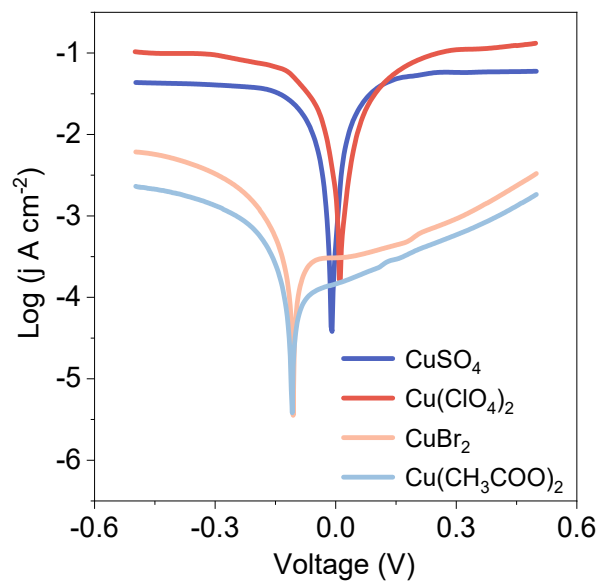


Fig. S21 Tafel curves of $\text{Cu}||\text{Cu}$ symmetric cells in different electrolytes.

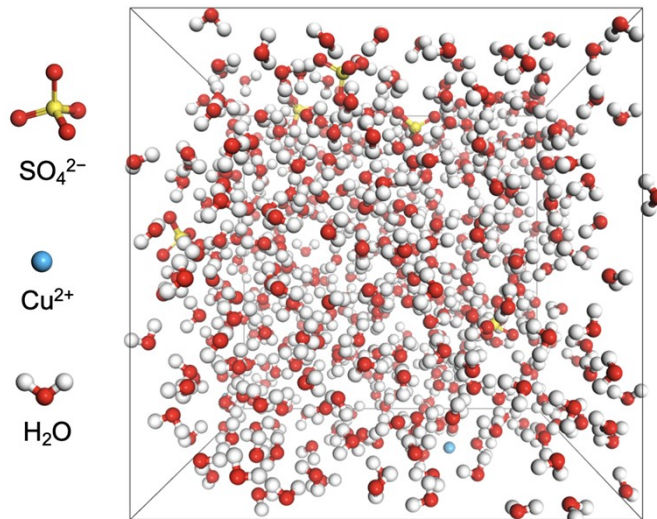


Fig. S22 3D snapshot of the 0.5 m CuSO₄ electrolyte.

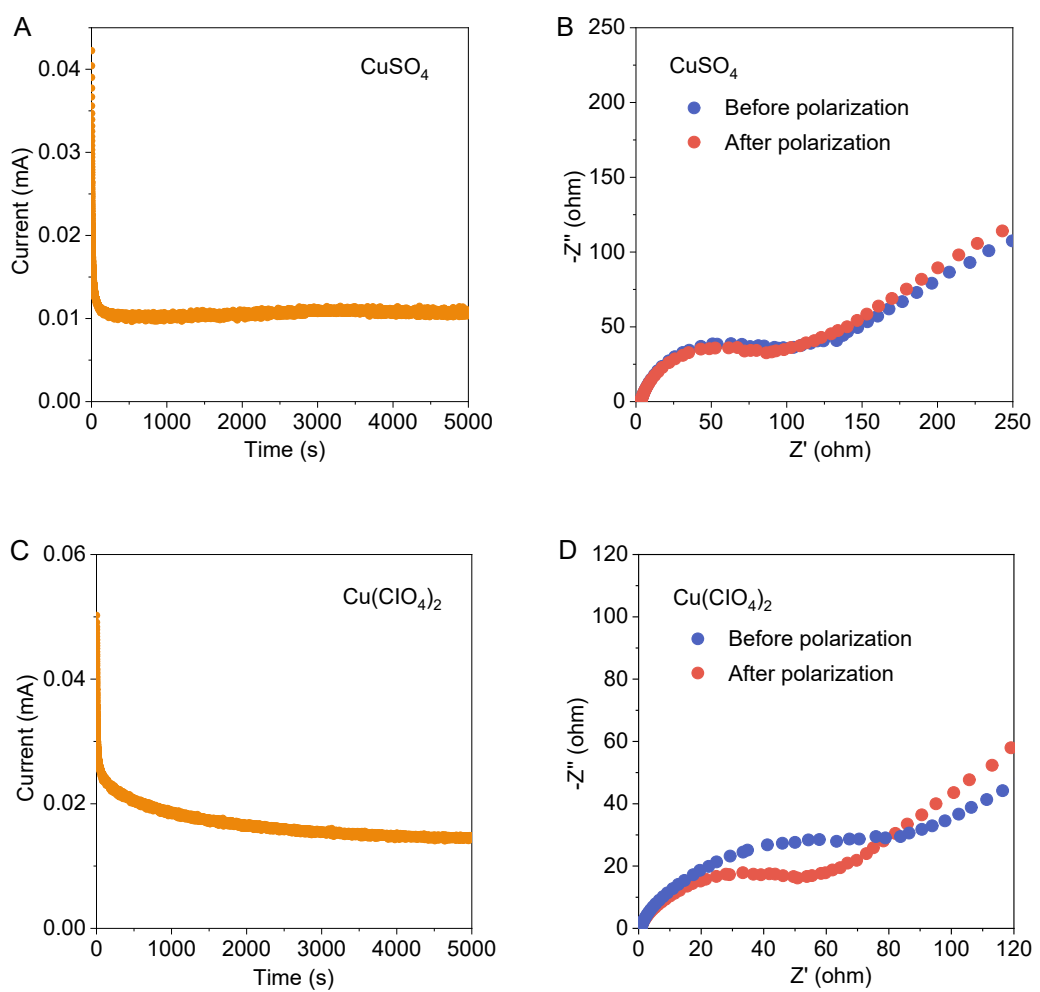


Fig. S23 Current-time plots of Cu symmetric cell in various electrolytes after polarization at a constant potential (25 mV) for 5000 s and the impedance spectra before and after the polarization.

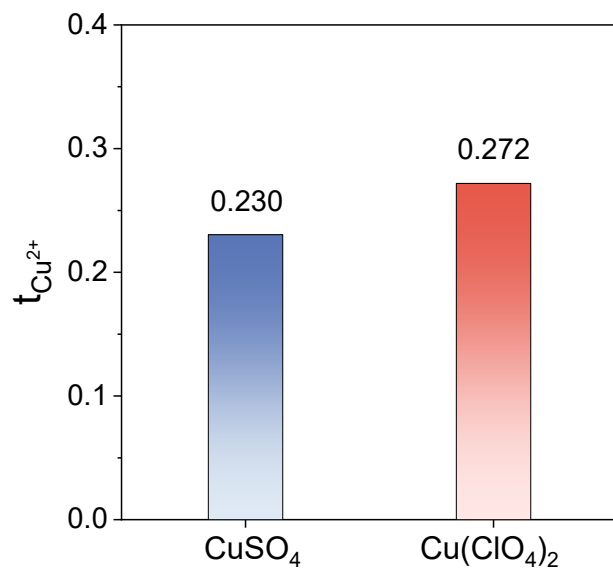


Fig. S24 The transference number of Cu^{2+} in different electrolytes.

The relatively low Cu^{2+} ion transference number is not in conflict with the high ionic conductivity of the electrolyte. The high ionic conductivity reflects the total mobility of all ions, while the relatively low Cu^{2+} ion transference number indicates that anions contribute significantly to the overall ion transport.

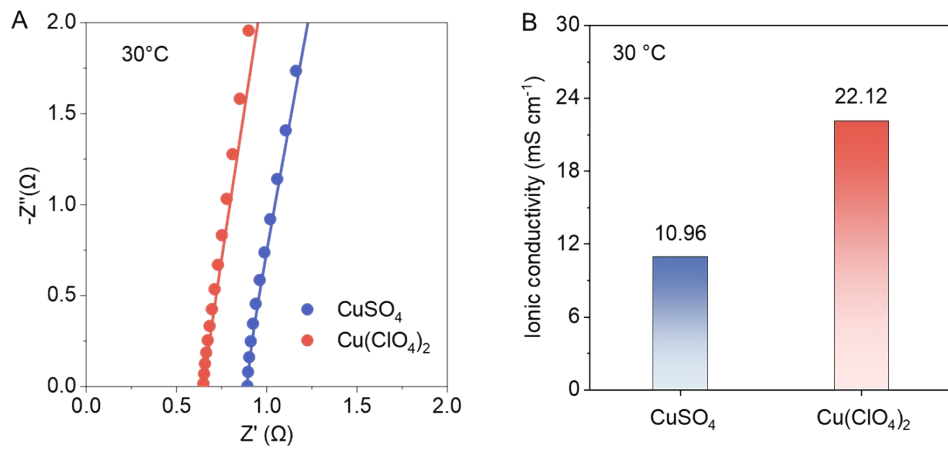


Fig. S25 (A) Nyquist plots obtained at open circuit voltage in different electrolytes. (B) Comparison of ionic conductivity of different electrolytes.

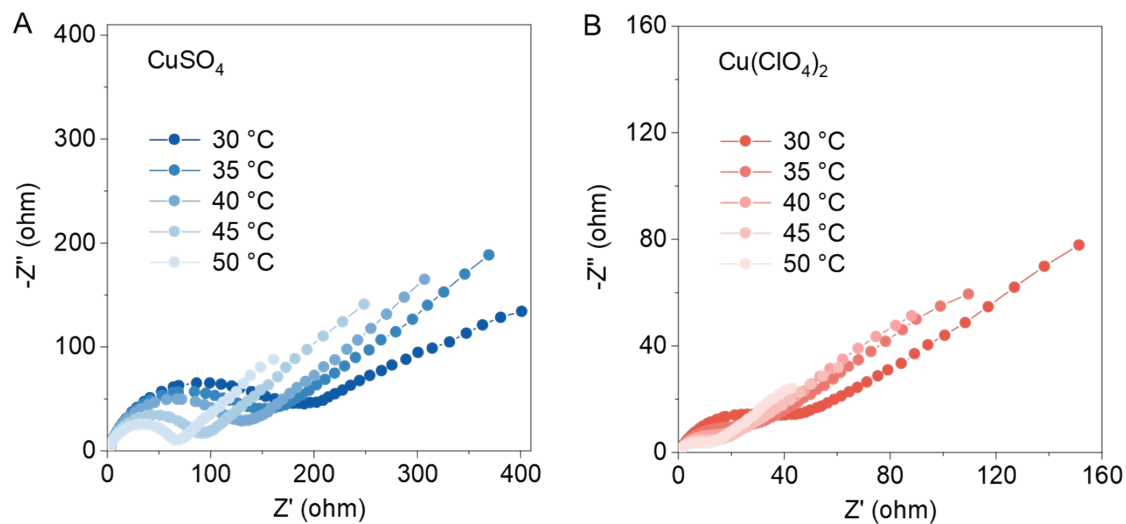


Fig. S26 Nyquist plots of Cu||Cu cells at different temperatures in (A) CuSO₄ and (B) Cu(ClO₄)₂ electrolytes.

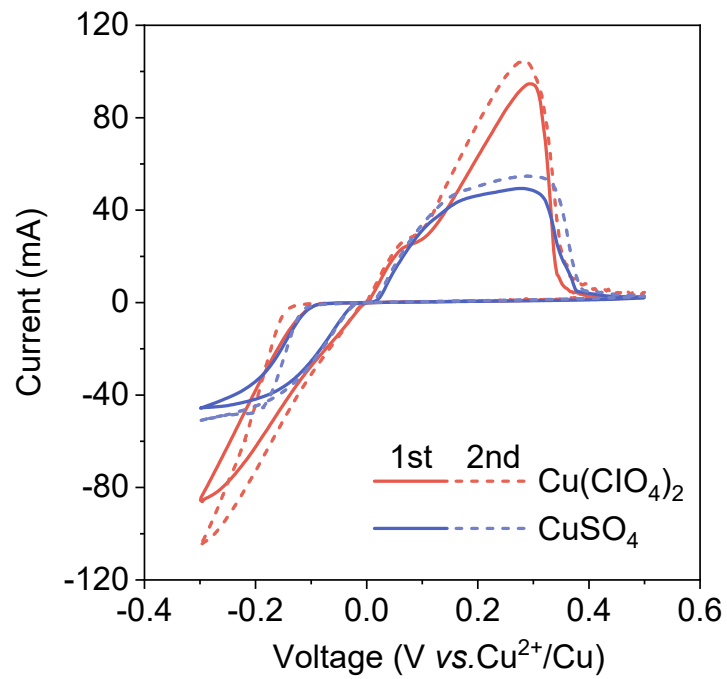


Fig. S27 CV curves of Cu||Ti cells in different electrolytes.

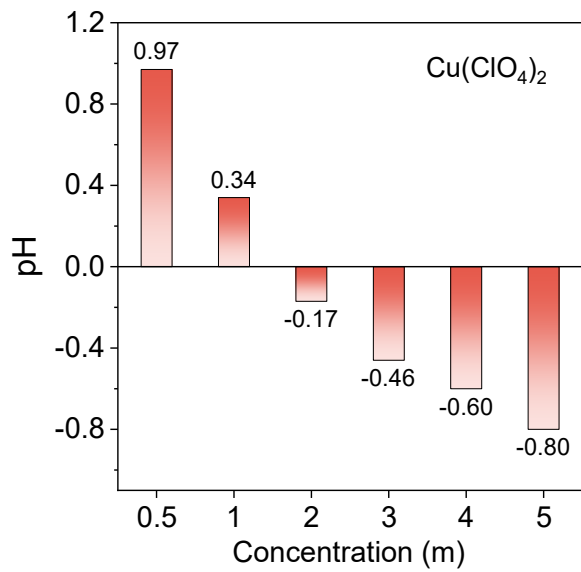


Fig. S28 pH of the electrolytes with varying concentration of Cu(ClO₄)₂.

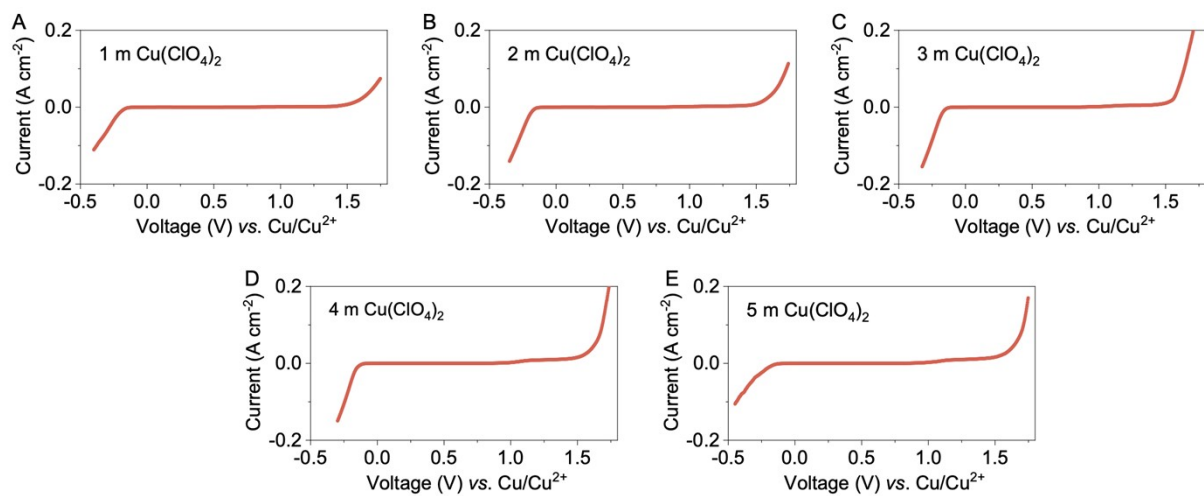


Fig. S29 LSV curves for electrochemical stability window of electrolytes with varying concentrations of $\text{Cu}(\text{ClO}_4)_2$ with a scan rate of 1 mV s^{-1} .

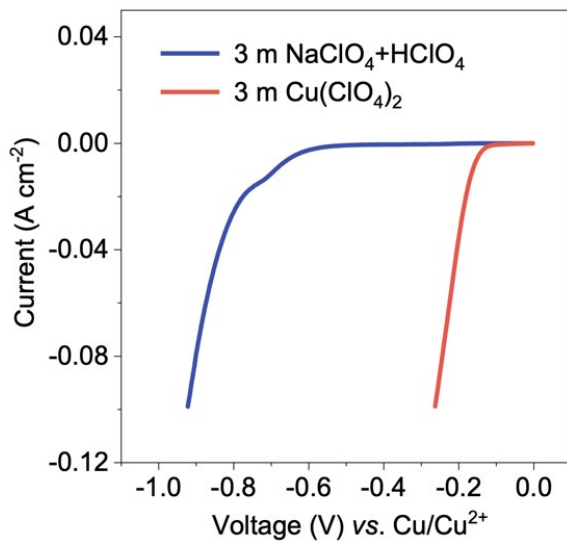


Fig. S30 LSV curves of Cu||Ti cells using 3 m NaClO₄ (pH value was adjusted to -0.46 using HClO₄) and 3 m Cu(ClO₄)₂ (pH: -0.46) electrolytes at a scan rate of 1 mV s⁻¹.

To investigate the effect of low pH on hydrogen evolution, HER tests were conducted using linear potential scan. To eliminate current interference from Cu²⁺ deposition, 3 m Cu(ClO₄)₂ was replaced with 3 m NaClO₄, and the pH of the NaClO₄ solution was adjusted using HClO₄ to match that of 3 m Cu(ClO₄)₂ (-0.46). The HER onset potential is much lower than the Cu²⁺ deposition potential, ensuring that Cu deposition/stripping occurs without interference from hydrogen evolution.

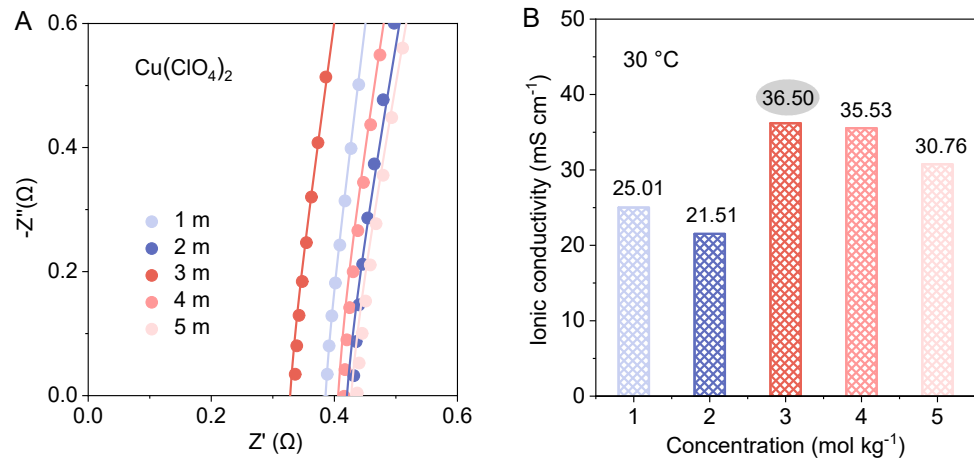


Fig. S31 (A) Nyquist plots obtained from EIS investigation. (B) Ionic conductivities of $\text{Cu}(\text{ClO}_4)_2$ electrolytes with different concentrations.

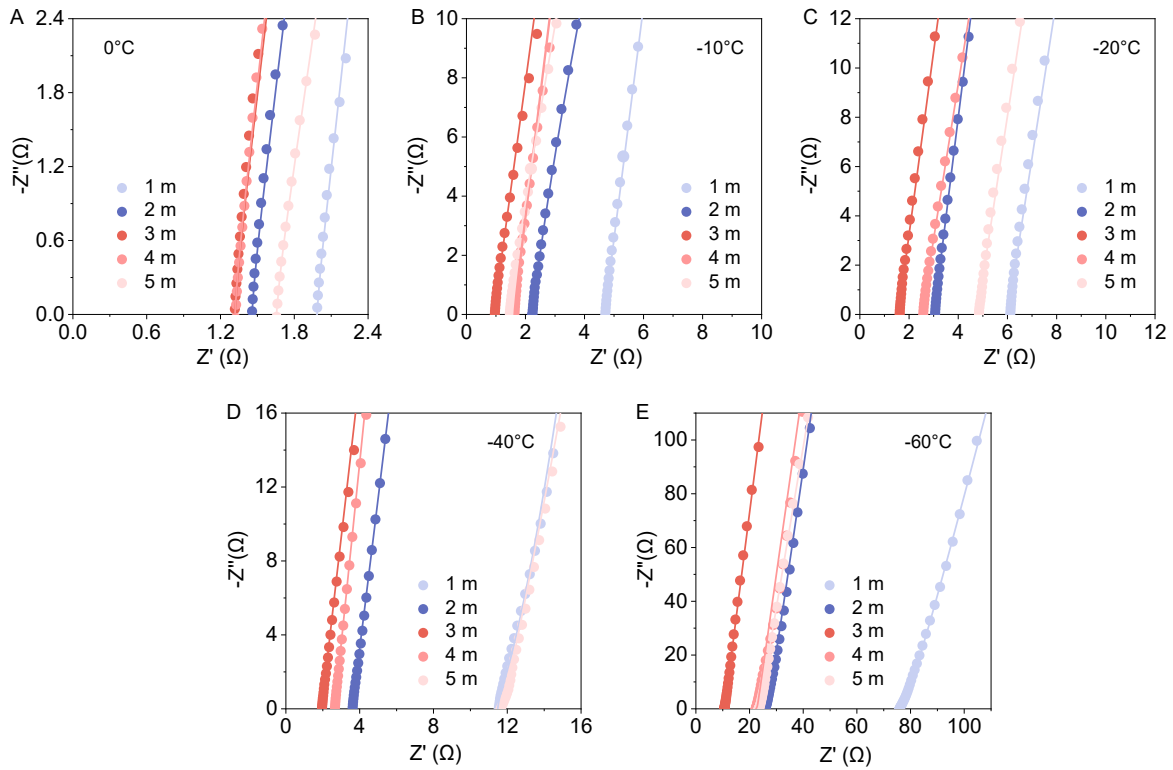


Fig. S32 Nyquist plots obtained from EIS investigation.

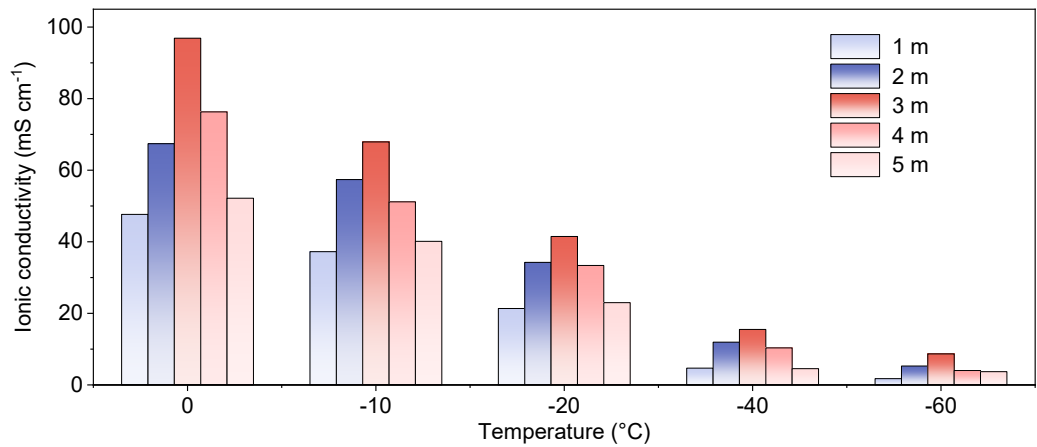


Fig. S33 The ionic conductivities of $\text{Cu}(\text{ClO}_4)_2$ electrolyte in the temperature range of $-60\text{--}0$ $^{\circ}\text{C}$.

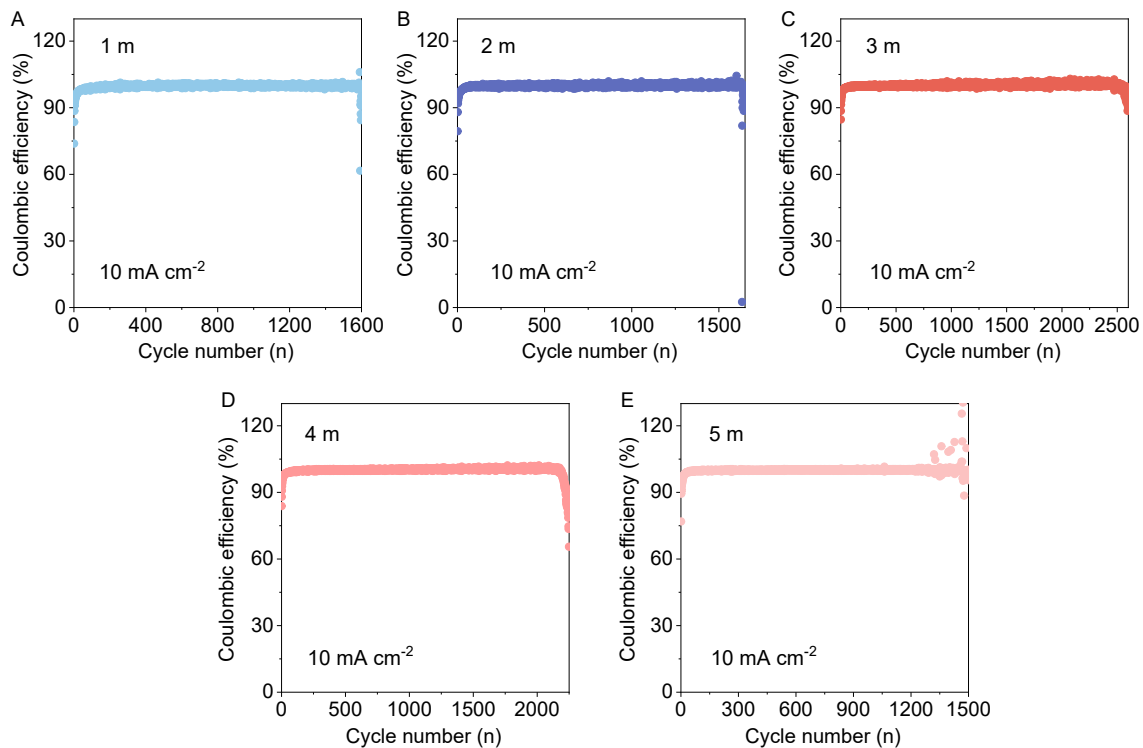


Fig. S34 Coulombic efficiency of Cu||Ti cells with different concentrations of $\text{Cu}(\text{ClO}_4)_2$ electrolytes.

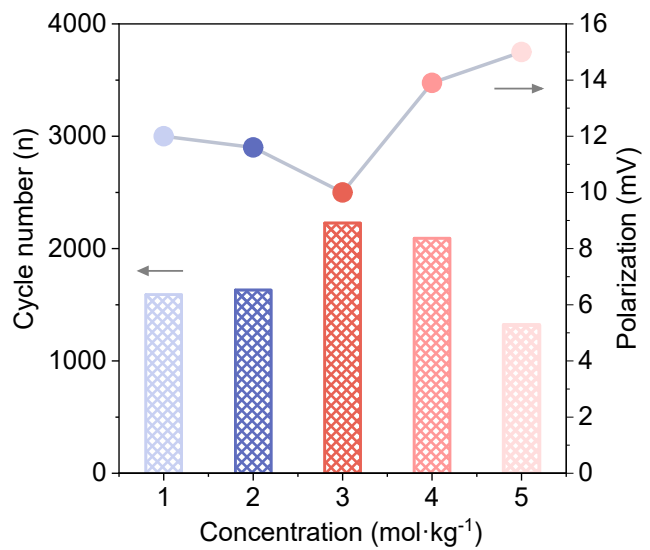


Fig. S35 Comparison of cycle life and polarization voltage of $\text{Cu}(\text{ClO}_4)_2$ electrolytes with different concentrations.

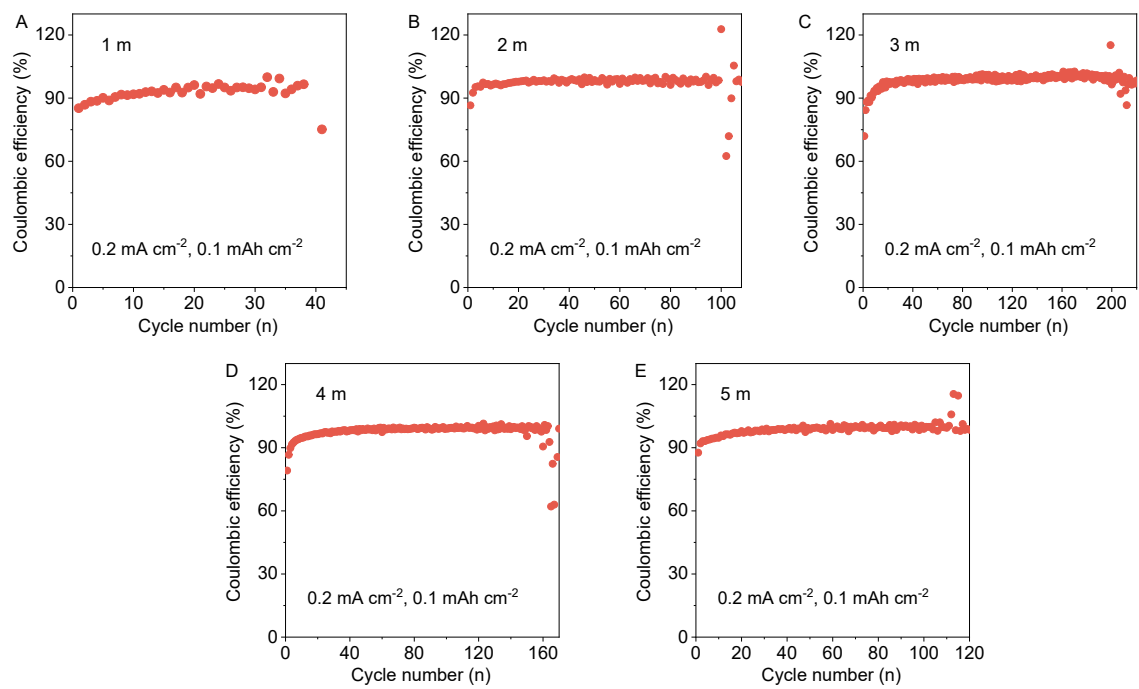


Fig. S36 Cycling performance of Cu||Ti asymmetric cells of the electrolytes with varying concentration of $\text{Cu}(\text{ClO}_4)_2$ at $-60\text{ }^{\circ}\text{C}$.

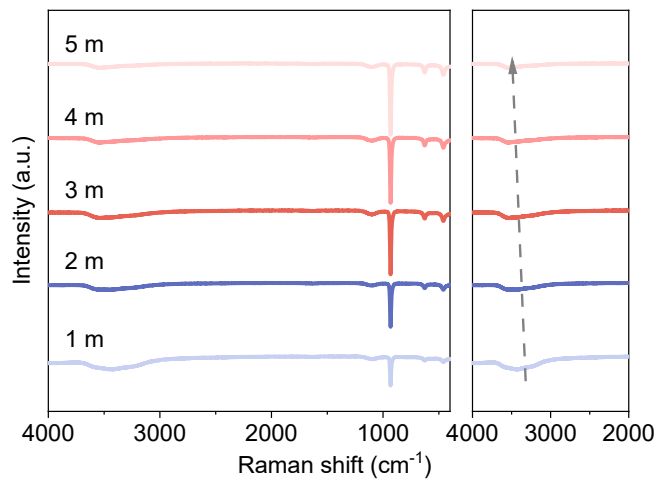


Fig. S37 Raman spectra of electrolytes with varying concentrations of $\text{Cu}(\text{ClO}_4)_2$.

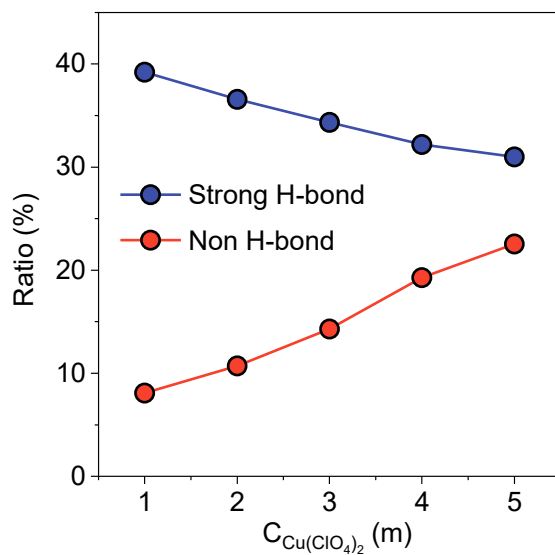


Fig. S38 The proportion of strong H-bond and non H-bond in varying concentrations of $\text{Cu}(\text{ClO}_4)_2$.

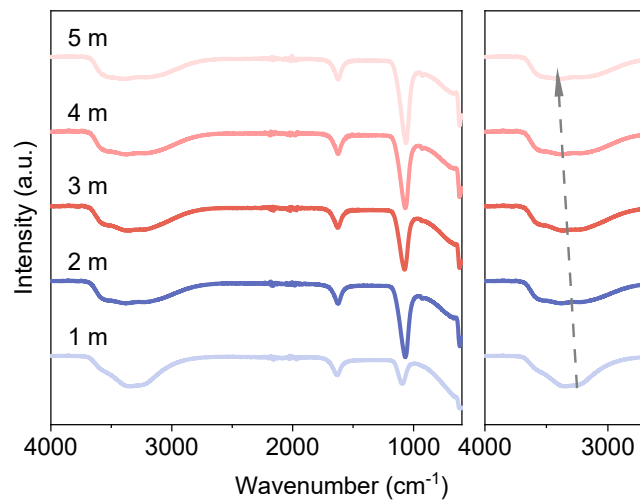


Fig. S39 FTIR spectra of electrolytes with varying concentrations of $\text{Cu}(\text{ClO}_4)_2$.

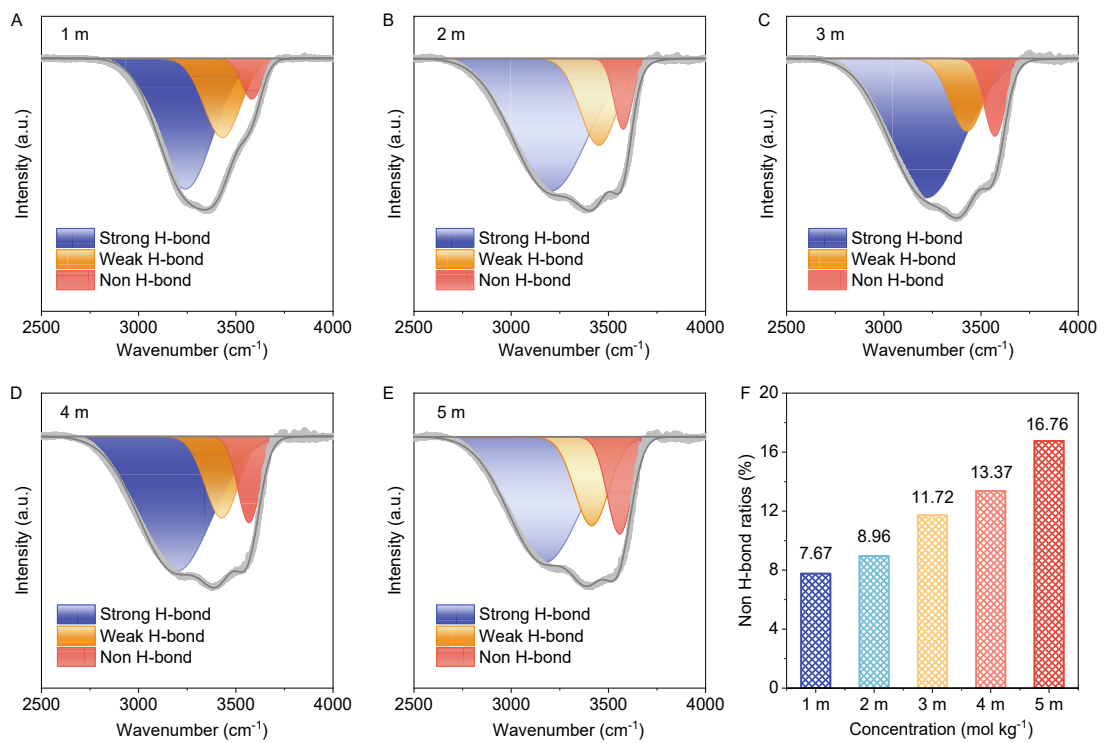


Fig. S40 The fitted FTIR peaks representing the O-H stretching vibration of water molecules in (A-E) electrolytes with different concentrations of $\text{Cu}(\text{ClO}_4)_2$. (F) The proportions of non H-bonds in the electrolytes.

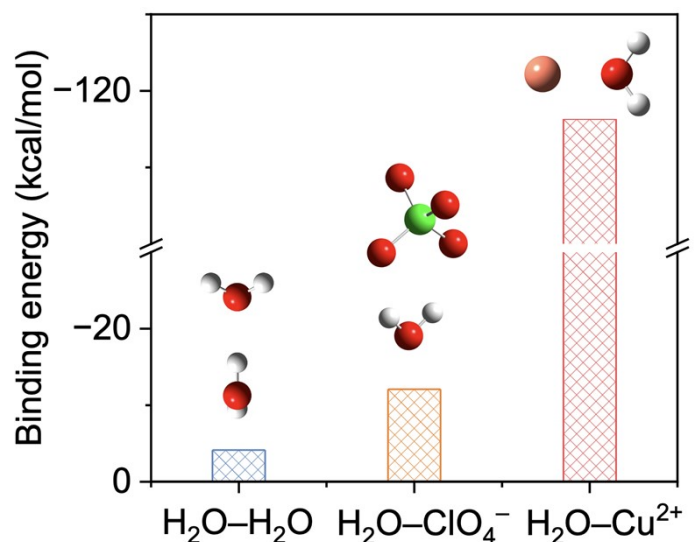


Fig. S41 The binding energies of H_2O with H_2O , ClO_4^- and Cu^{2+} .

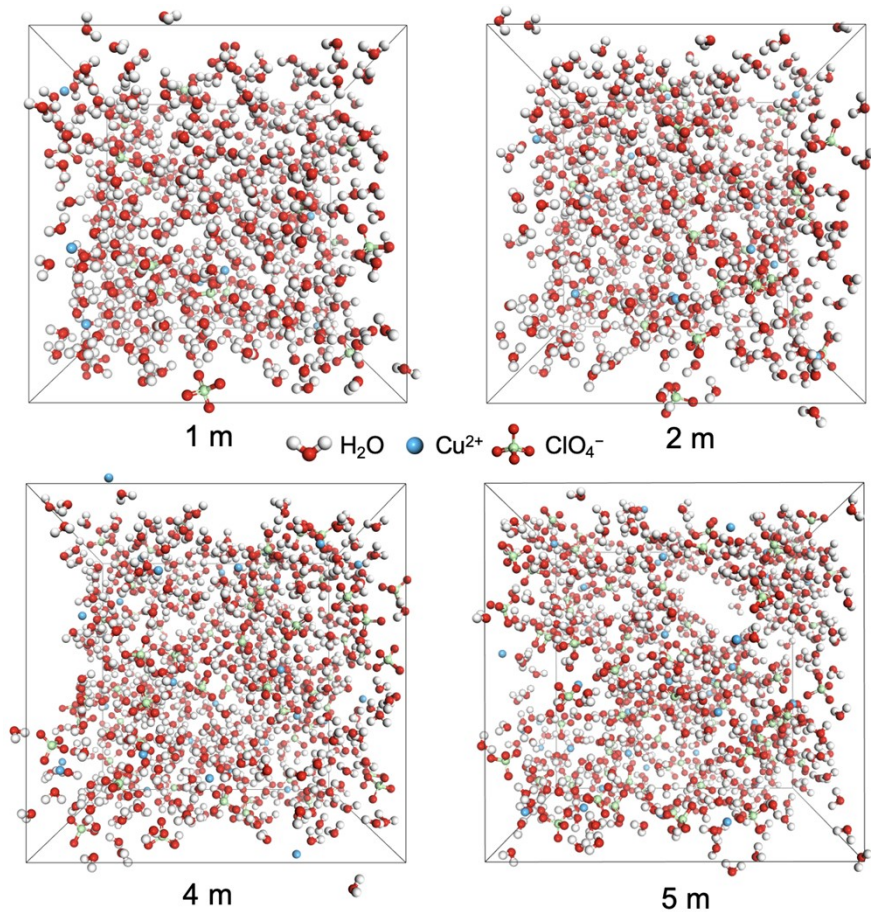


Fig. S42 3D snapshot of Cu(ClO₄)₂ electrolyte at various concentrations.

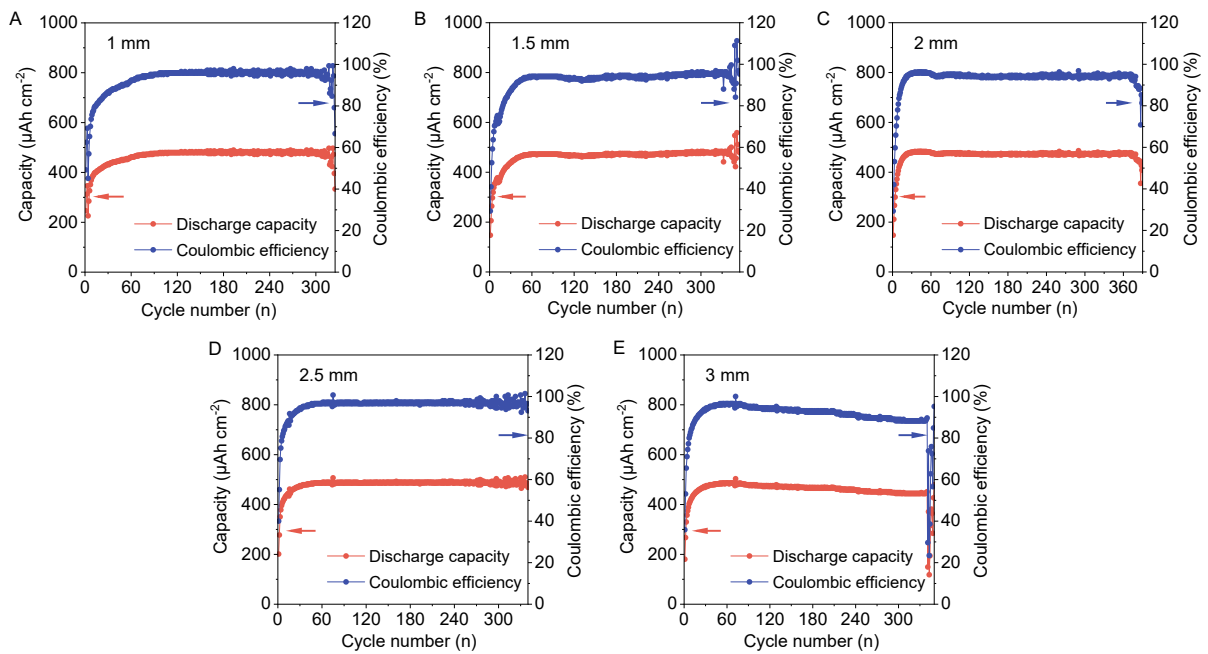


Fig. S43 Cycling performance of Cu-MnO₂ batteries with different thickness of the hydrogel.

The cycling stability and Coulombic efficiency of the batteries remain virtually unaffected within the range of hydrogel thickness. However, excessively thick hydrogels can complicate the encapsulation of planar micro-batteries. Therefore, a thickness of around 2 mm is optimal for both electrochemical performance and micro-battery assembly.

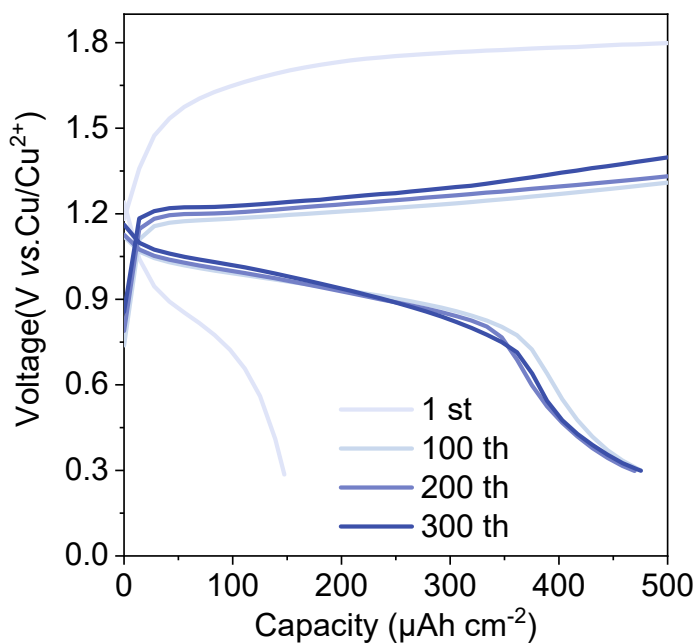


Fig. S44 Voltage profiles of Cu||MnO₂ cells at a current density of 10 mA cm⁻².

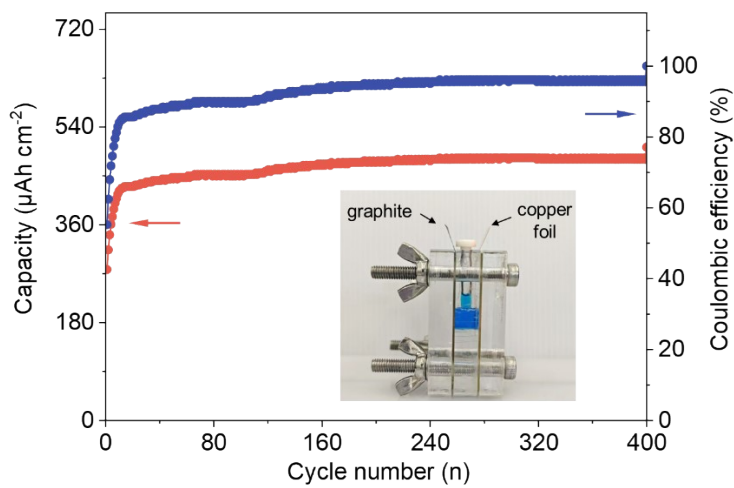


Fig. S45 The cycle performance of the Cu-MnO₂ full cell using 3 m Cu(ClO₄)₂ and 1 m Mn(ClO₄)₂ aqueous solution (inset: photographic picture of the Cu-MnO₂ full cell).

To exclude the effect of hydrogel on cycling performance, the cycling performance of the dual-plating Cu-MnO₂ battery was tested using an aqueous solution (3 m Cu(ClO₄)₂ and 1 m Mn(ClO₄)₂). The Cu-MnO₂ micro-battery demonstrated stable cycling performance over 400 cycles at a current density of 10 mA cm⁻².

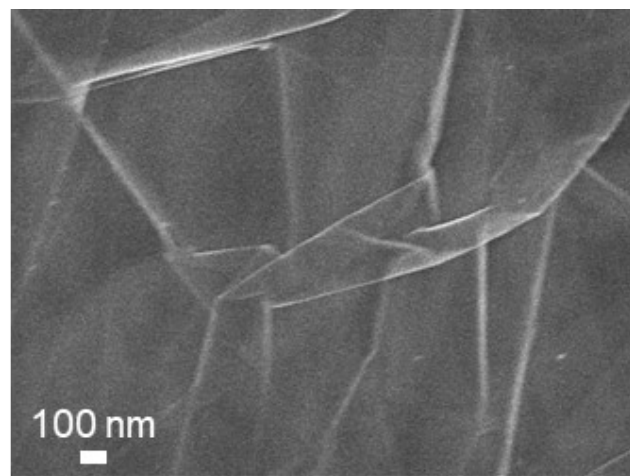


Fig. S46 SEM image of commercial graphite paper.

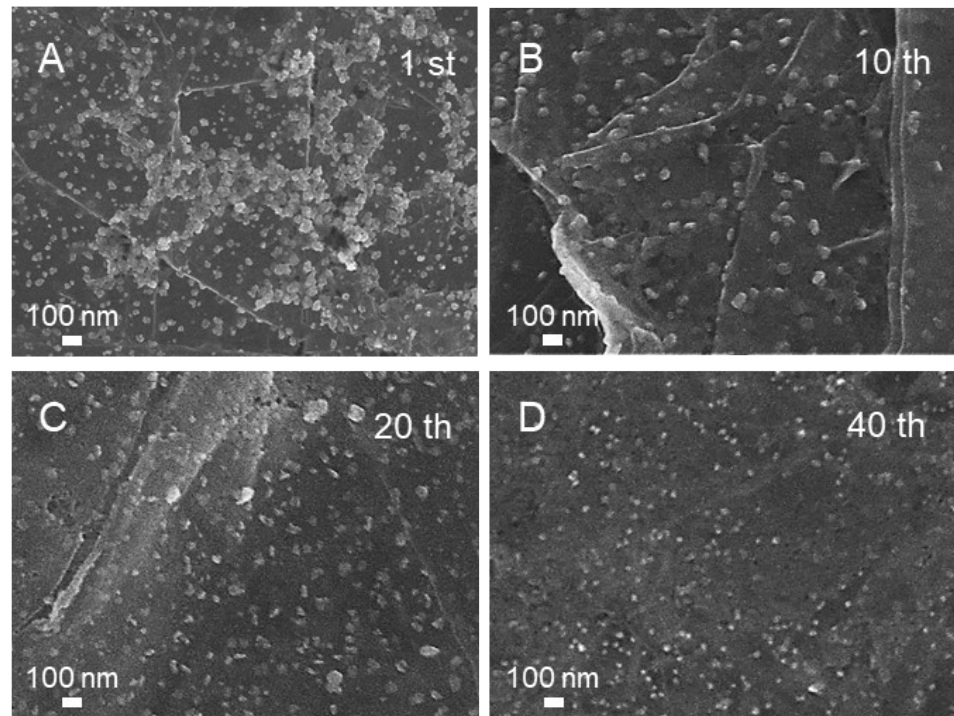


Fig. S47 SEM images of MnO₂ particles deposited on graphite paper at different cycles.

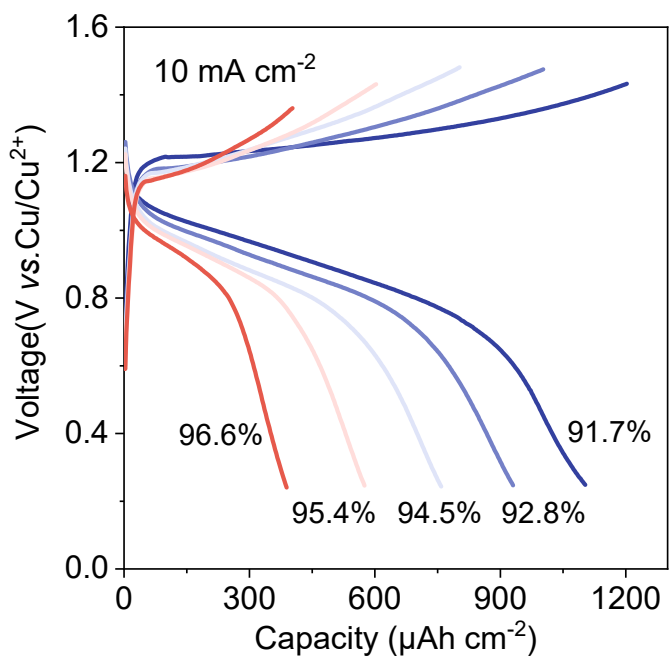


Fig. S48 Coulombic efficiencies of Cu||MnO₂ cells at different charge capacities.

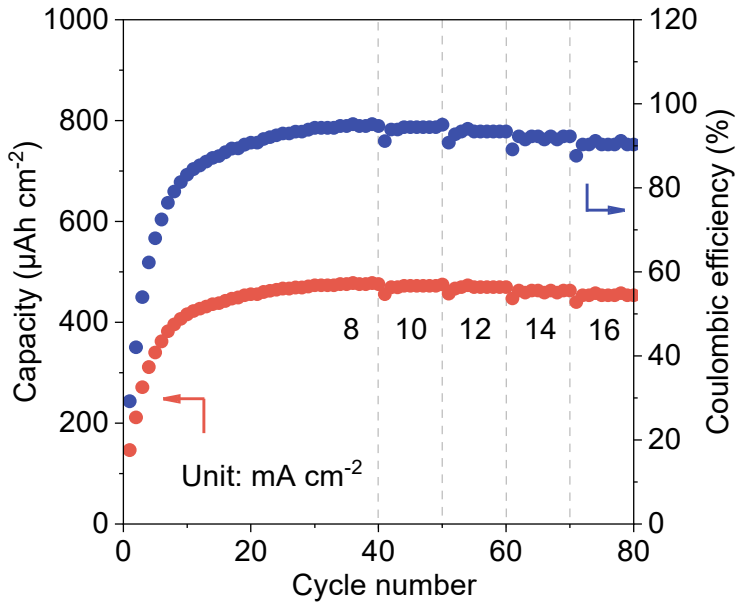


Fig. S49 Rate performance of Cu-MnO₂ batteries at current densities from 8 to 16 mA cm^{-2} .

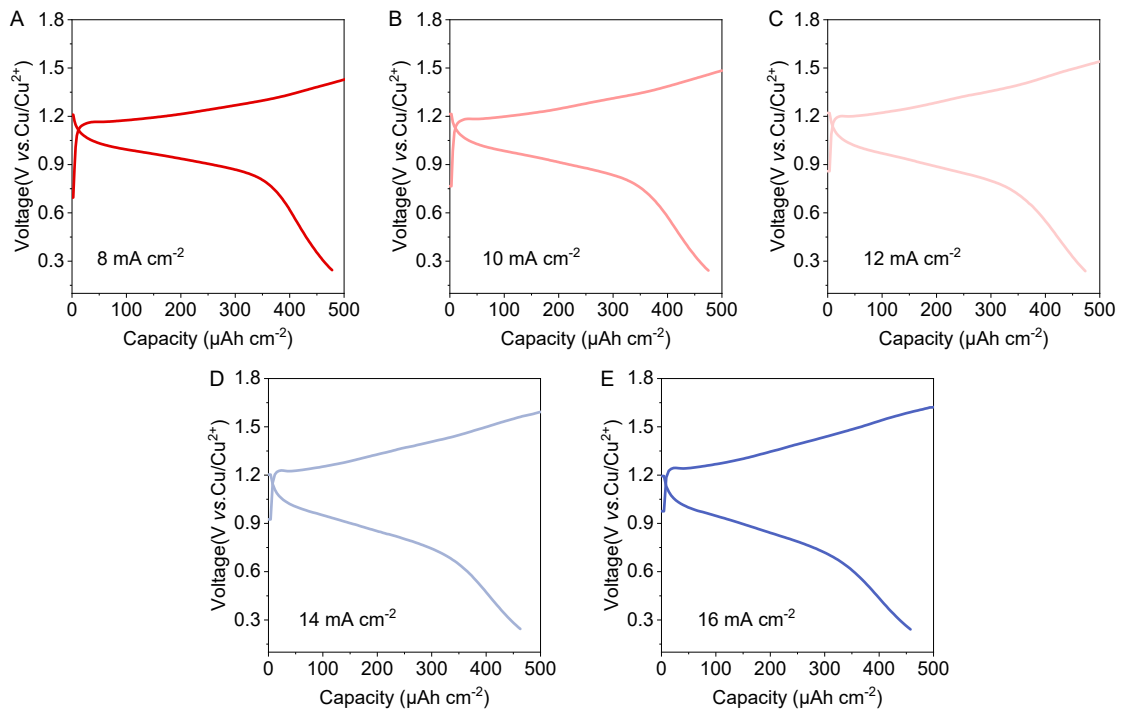


Fig. S50 Voltage profiles of $\text{Cu}||\text{MnO}_2$ cells at different current densities.

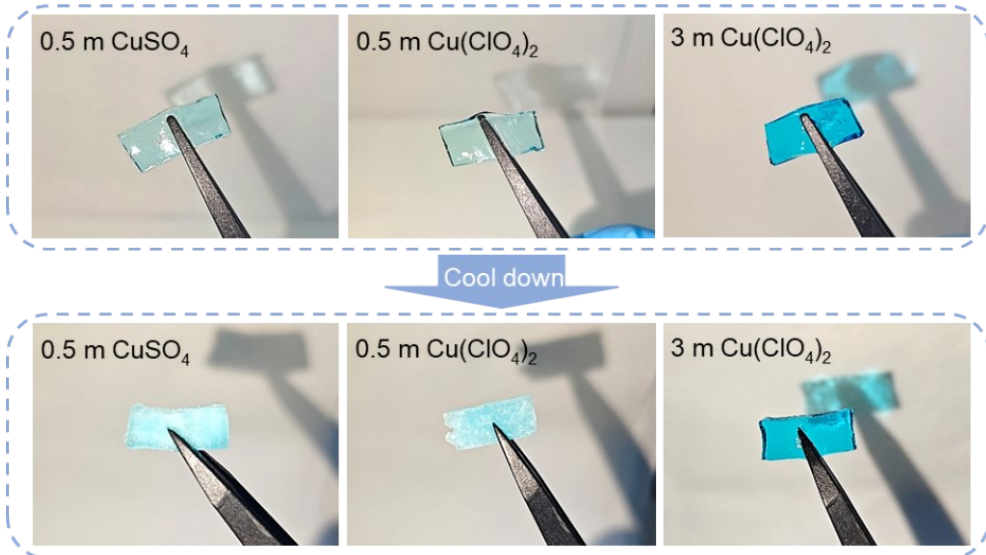


Fig. S51 The optical photographs of the hydrogel with different electrolytes at 25 °C and -60 °C.

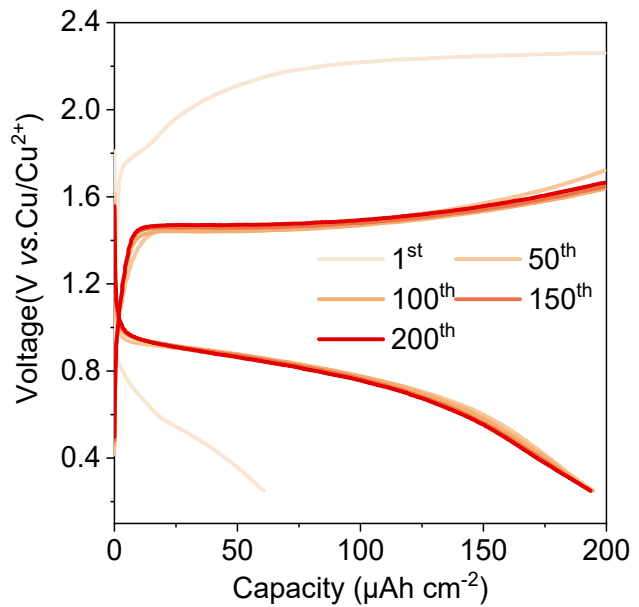


Fig. S52 Voltage profiles of Cu|MnO₂ cells at -60 °C for different cycles.

Table S1. Comparison of the cycling performance of Cu||Cu symmetric cells in various electrolytes.

Electrode	Current density	Capacity	Electrolyte	Cycle life	Polarization	Ref.
Cu	1 mA cm ⁻²	1 mA h cm ⁻²	0.5 m Cu(ClO ₄) ₂	7000 h	11 mV	This work
	10 mA cm ⁻²	1 mA h cm ⁻²	0.5 m Cu(ClO ₄) ₂	1000 h	32 mV	This work
Cu	1 mA cm ⁻²	1 mA h cm ⁻²	0.05 m MKP +1 m CuSO ₄	2800 h	94.8 mV	Ref. 9
Cu	1 mA cm ⁻²	1 mA h cm ⁻²	CuSO ₄ + H ₂ SO ₄ (pH = 1)	1200 h	56 mV	Ref. 10
Cu	0.5 mA cm ⁻²	—	30 m ChCl + 1 m CuCl ₂	1500 h	100 mV	Ref. 11
Cu/Ni	2 mA cm ⁻²	0.5 mA h cm ⁻²	2 m H ₂ SO ₄ + 0.5 m CuSO ₄	300 h	70 mV	Ref. 12
CP@PAN @Cu	0.5 mA cm ⁻²	1 mA h cm ⁻²	0.5 m CuSO ₄	1200 h	30 mV	Ref. 13
Cu	0.2 mA cm ⁻²	0.2 mA h cm ⁻²	4 m Cu(BF ₄) ₂	730 h	50 mV	Ref. 14
Cu	0.5 mA cm ⁻²	0.5 mAh cm ⁻²	4 m Cu(BF ₄) ₂ + 1 m H ₃ PO ₄	720 h	46 mV	Ref. 15
Cu	10 mA cm ⁻²	1 mA h cm ⁻²	6.82 m LiCl + 0.1 m CuCl + 1.64 m AlCl ₃	8.3 h	80 mV	Ref. 16

Table S2. Comparison of Corrosion potential and corrosion density of Cu in different electrolytes.

Electrolyte	Corrosion potential (V)
CuSO ₄	-0.0090
Cu(ClO ₄) ₂	0.0108
CuBr ₂	-0.1058
Cu(CH ₃ COO) ₂	-0.1082

Table S3. Ionic conductivities of Cu(ClO₄)₂ electrolyte in the temperature range of -60~0 °C.

Temperature (°C)	Ionic conductivity (mS cm ⁻¹)				
	1 m	2 m	3 m	4 m	5 m
0	47.6	67.4	96.9	76.3	52.1
-10	37.2	57.3	67.9	51.1	40.1
-20	21.3	34.2	41.4	33.3	22.9
-40	4.7	11.9	15.5	10.3	4.5
-60	1.7	5.2	8.6	4.0	3.7

Table S4. Comparison of electrochemical performance of aqueous Cu-based batteries.

Electrode	Electrolyte	Current Density	Durability	Decay rate per cycle	Voltage	Ref.
Cu-MnO ₂	3 m Cu(ClO ₄) ₂ + 1 m Mn(ClO ₄) ₂	10 mA cm ⁻²	370	0.004%	0.9 V	This work
Cu Se@C	0.5 m CuSO ₄	5 A g ⁻¹	300	0.017%	0.16 V	Ref. 17
Cu-Zn	1 m KOH	1 A g ⁻¹	200	0.27%	0.75 V	Ref. 18
Cu-CuFe PBA	0.2 m CuSO ₄ + 0.5 m H ₂ SO ₄	1.36 mA cm ⁻²	100	0.041%	0.75 V	Ref. 19
Cu-S	0.5 M CuSO ₄	0.5 A g ⁻¹	150	0.1067%	0.46 V	Ref. 20
Cu-Al	6.82 m LiCl + 0.1 m CuCl + 1.64 m AlCl ₃	1 A g ⁻¹	200	0.0588%	0.3 V	Ref. 16
Cu-AC	4.5 m K ₂ CO ₃ + 9 m KOH	500 mA g ⁻¹	50	0.30%	0.3 V	Ref. 21
Cu-Zn	1.0 m ZnSO ₄	100 mA g ⁻¹	110	0.1319%	0.85 V	Ref. 22
Cu/Bi@C-Zn	45 wt.% KOH	170 mA g ⁻¹	200	0.09523%	0.7 V	Ref. 23
Cu-Zn	15 m ZnCl ₂ + organic phase	800 mA g ⁻¹	100	0.05128%	0.7, 1.3 V	Ref. 24
Cu-S	0.5 M CuSO ₄	0.8 A g ⁻¹	328	0.02675%	0.15 V	Ref. 25
Cu-V ₂ O ₅	0.5 M CuSO ₄	0.5 A g ⁻¹	100	0.2174%	0.1 V	Ref. 26

Table S5. The numbers of water molecules and ions in amorphous cell module.

Electrolyte	H ₂ O	Cu ²⁺	M ⁻	SO ₄ ²⁻
0.5 m CuSO ₄	500	5	—	5
0.5 m Cu(ClO ₄) ₂	500	5	10	—
0.5 m CuBr ₂	500	5	10	—
0.5 m Cu(CH ₃ COO) ₂	500	5	10	—
1 m Cu(ClO ₄) ₂	500	10	20	—
2 m Cu(ClO ₄) ₂	500	20	40	—
3 m Cu(ClO ₄) ₂	500	30	60	—
4 m Cu(ClO ₄) ₂	500	40	80	—
5 m Cu(ClO ₄) ₂	500	50	100	—

References

- 1 H. Sun, *J. Phys. Chem.*, 1998, **102**, 7338–7364.
- 2 H. Sun, P. Ren and J. R. Fried, *COMP. AND THEOR. POLYMER SCIENCE.*, 1998, **8**, 229–246.
- 3 L. Yao, Z. Qin, Q. Chen, M. Zhao, H. Zhao, W. Ahmad, L. Fan and L. Zhao, *Sep. Purif. Technol.*, 2018, **205**, 48–57.
- 4 Frisch, M. J., et al., *Gaussian 16*. Gaussian, Inc. Wallingford CT, 2016.
- 5 F. J. Devlin, J. W. Finley, P. J. Stephens and M. J. Frisch, *J. Phys. Chem.*, 1995, **99**, 16883–16902
- 6 P. J. Hay and W. R. Wadt, *J. Chem. Phys.*, 1985, **82**, 270–283.
- 7 P. J. Hay and W. R. Wadt, *J. Chem. Phys.*, 1985, **82**, 299–310.
- 8 A. D. McLean and G. S. Chandler, *J. Chem. Phys.*, 1980, **72**, 5639–5648.
- 9 Y. Sun, Z. Yao, Q. Lei, Y. Zhao, Z. Ren, W. Zhang, J. Si, L. Zhang, W. Wen, D. Zhu, X. Li and R. Tai, *Adv. Mater.*, 2023, **35**, 2305087.
- 10 Z. He, J. Guo, F. Xiong, S. Tan, Y. Yang, R. Cao, G. Thompson, Q. An, M. De Volder and L. Mai, *Energy Environ. Sci.*, 2023, **16**, 5832–5841.
- 11 Z. Duan, J. Zhao, Y. Qi, R. Li, W. Wang, Q. Peng, S. Han and L. Zhang, *Chem. Commun.*, 2022, **58**, 10076–10079.
- 12 H. Cai, S. Bi, R. Wang, L. Liu and Z. Niu, *Angew. Chem., Int. Ed.*, 2022, **61**, e202205472.
- 13 H. Yan, Z. Yang, C. Xu, J. Li, Y. Liu, R. Zheng, H. Yu, L. Zhang and J. Shu, *Energy Storage Mater.*, 2022, **48**, 74–81.
- 14 C. Yan, Z. Chen, H. Huang and X. Deng, *Angew. Chem., Int. Ed.*, 2023, **62**, e202300523.
- 15 C. Yan, Z. Chen, H. Deng, H. Huang and X. Deng, *J. Energy Chem.*, 2023, **80**, 758–767.
- 16 M. Tan, Y. Qin, Y. Wang, F. Zhang and X. Lei, *Sci. Rep.*, 2022, **12**, 18714.
- 17 C. Dai, L. Hu, H. Chen, X. Jin, Y. Han, Y. Wang, X. Li, X. Zhang, L. Song, M. Xu, H. Cheng, Y. Zhao, Z. Zhang, F. Liu and L. Qu, *Nat. Commun.*, 2022, **13**, 1863.
- 18 Q. Zhu, M. Cheng, B. Zhang, K. Jin, S. Chen, Z. Ren and Y. Yu, *Adv. Funct. Mater.*, 2019, **29**, 1905979.
- 19 G. Liang, F. Mo, Q. Yang, Z. Huang, X. Li, D. Wang, Z. Liu, H. Li, Q. Zhang and C. Zhi, *Adv. Mater.*, 2019, **31**, 1905873.

- 20 J. Zhang, Y. Wang, M. Yu, J. Ni and L. Li, *ACS Energy Lett.*, 2022, **7**, 1835–1841.
- 21 T. C. Gallagher, C. Y. Wu, M. Lucero, S. K. Sandstrom, L. Hagglund, H. Jiang, W. Stickle, Z. Feng and X. Ji, *Angew. Chem., Int. Ed.*, 2022, **61**, e202203837.
- 22 J. F. F. Gomez, N. Oli, S. Chang, S. Qiu, S. Katiyar, R. Katiyar, G. Morell and X. Wu, *ACS Appl. Energy Mater.*, 2024, **7**, 2048–2056.
- 23 D. J. Arnot, N. B. Schorr, I. V. Kolesnichenko and T. N. Lambert, *J. Power Sources*, 2022, **529**, 231168.
- 24 C. Xu, C. Lei, J. Li, X. He, P. Jiang, H. Wang, T. Liu and X. Liang, *Nat. Commun.*, 2023, **14**, 2349.
- 25 Z. Yang, C. Xu, H. Yan, Y. Liu, C. Yue, L. Zhang, M. Shui, F. Hu and J. Shu, *Adv. Funct. Mater.*, 2021, **31**, 2103893.
- 26 Y. Jiang, J. Lu, A. Xiang, X. Zhang, D. Liu, Z. Yang and P. Hu, *Batteries*, 2023, **9**, 572.